

**HOMOGENIZATION STUDIES FOR
OPTICAL SENSORS BASED ON
SCULPTURED THIN FILMS**

Siti Suhana Jamaian



Doctor of Philosophy
University of Edinburgh
2012

Declaration

I declare that this thesis was composed by myself and that the work contained therein is my own, except where explicitly stated otherwise in the text.

(Siti Suhana Jamaian)



PTTA UTHM
PERPUSTAKAAN TUNKU TUN AMINAH

To my love

Abd Fathul Hakim Zulkifli

Faheem Irsyad Abd Fathul Hakim



PTTA UTHM
PERPUSTAKAAN TUNKU TUN AMINAH

Acknowledgements

I would like to express my sincere gratitude to my research supervisor, Dr. Tom G. Mackay who has served not only as a supervisor but also encouraged and motivated me throughout my research study. His wide knowledge and logical way of thinking have been of great value for me. Without his continuous support, this thesis would not be the same as presented here.

I am also very thankful to my family for giving me great supports especially my mum who keep pushing me to finish this study on time. To my son, Faheem Irsyad who always makes me laugh with his cute funny face whenever I tired and depressed with my work. My special thanks also dedicated to my lovely husband Abd Fathul Hakim who sacrificed not only his career but also everything to make sure I could finish this research study.

My sincere appreciation also extends to my second supervisor Dr. Nikola Popovic, lecturers, all my friends and others who have provided assistance at various occasions. Their views and tips are useful indeed. Only God can repay all their contributions.

And most especially to God, who made all things possible. *Alhamdulillah.*

Abstract

In this thesis we investigate theoretically various types of sculptured thin film (STF) envisioned as platforms for optical sensing. A STF consists of an array of parallel nanowires which can be grown on a substrate using vapour deposition techniques. Typically, each nanowire has a diameter in the range from $\sim 10 - 300$ nm while the film thickness is $\lesssim 1\mu\text{m}$. Through careful control of the fabrication process, both the optical properties and the porosity of the STF can be tailored to order. These abilities make STFs promising for optical sensing applications, wherein it is envisaged that the material to be sensed infiltrates the void region in between the parallel nanowires and hence changes the optical properties of the STF. Various homogenization formalisms can be used to estimate the constitutive parameters of the infiltrated STFs. In this thesis two different homogenization formalisms were used: the Bruggeman formalism (extended and non-extended versions) and the strong-permittivity-fluctuation theory (SPFT). These were used in investigations of the following optical-sensing scenarios: (i) Electromagnetic radiation emitted by a dipole source inside an infiltrated chiral STF. The effects of using the extended Bruggeman homogenization formalism, which takes into account the nonzero size of the component particles, were studied. (ii) Surface-plasmon-polariton waves on a metal-coated, infiltrated columnar thin film. The influences of using the extended SPFT formalism, which takes into account the nonzero size of the component particles and their statistical distributions, were explored. (iii) A metal-coated infiltrated chiral STF which supports both surface-plasmon-polariton waves and the circular Bragg phenomenon. The possibility of using in parallel both surface-plasmon-polariton waves and the circular Bragg phenomenon was investigated using the non-extended Bruggeman formalism. Our numerical studies revealed that the design performance parameters of the infiltrated STF are bode well for these optical-sensing scenarios. The use of inverse Bruggeman formalism was also investigated: this was found to be problematic in certain constitutive parameter regimes, but not those for optical-sensing scenarios considered in this thesis.

Publications and Presentations

The work described herein has to date yielded in the following refereed journal papers:

- J1. S. S. Jamaian and T. G. Mackay, On limitations of the Bruggeman formalism for inverse homogenization, *J. Nanophoton.* 4 (2010) 043510-1–043510-7.
- J2. S. S. Jamaian and T. G. Mackay, On chemiluminescent emission from an infiltrated chiral sculptured thin film, *Opt. Commun.* 284 (2011) 2382–2392. Erratum: 284 (2011) 3488.
- J3. S. S. Jamaian and T. G. Mackay, On columnar thin films as platforms for surface–plasmonic–polaritonic optical sensing: Higher–order considerations, *Opt. Commun.* 285 (2012) 5535–5542.

and the following conference papers:

- C1. S. S. Jamaian and T. G. Mackay, On dipole emission from an infiltrated chiral sculptured thin film, *Proc. SPIE* 8104 (2011) 81040F-1–81040F-9.
- C2. T. G. Mackay, A. Lakhtakia and S. S. Jamaian, Chiral sculptured thin films as integrated dual–modality optical sensors, *Proc. SPIE* (At press).

as well as the following poster presentations:

- P1. S. S. Jamaian and T. G. Mackay, A columnar thin film as a surface–plasmonic–polaritonic optical sensor, *Photon 12*, 3–6 September 2012, Durham University, Durham, UK.
- P2. S. S. Jamaian and T. G. Mackay, On sculptured thin film as platforms for optical sensing, *EOS Annual Meeting*, 25–28 September 2012, Aberdeen Exhibition and Conference Centre, Scotland, UK.

Contents

Acknowledgements	iv
Abstract	v
Publications and Presentations	vi
Contents	ix
List of Acronyms and Symbols	xii
List of Figures	xvii
1 Introduction	1
1.1 Background of Research	1
1.2 Objectives of Research	2
1.3 Importance of Research	2
1.4 Framework of Research	2
2 Homogenization formalisms	5
2.1 Introduction	5
2.2 The Maxwell Equations and Constitutive Relations	5
2.3 Depolarization dyadic	8
2.4 Distributional statistics	10
2.5 Homogenization formalisms	11
2.5.1 Preliminaries	11
2.5.2 Maxwell Garnett formalism	11
2.5.3 Bruggeman formalism	12
2.5.4 Strong Property Fluctuation theory	13
2.6 Conclusion	15

3 The Bruggeman formalism for inverse homogenization	16
3.1 Theory	17
3.2 Numerical studies	18
3.3 Closing remarks	21
4 Sculptured thin films	23
4.1 Introduction	23
4.2 Columnar thin films	23
4.3 Chiral sculptured thin films	25
4.4 Homogenization studies on STF's	26
4.4.1 Macroscopic perspective	26
4.4.2 Nanostructural perspective	28
4.4.3 Inverse homogenization — uninfiltrated STF	29
4.4.4 Forward homogenization — infiltrated STF	29
4.5 Conclusions	30
5 Dipole emission from an infiltrated chiral sculptured thin film	31
5.1 Introduction	31
5.2 Constitutive parameters of an infiltrated CSTF	32
5.3 Radiation from dipole source inside an infiltrated CSTF	36
5.3.1 Spectral Green function formulation	36
5.3.2 Boundary value problem	38
5.3.3 Emitted far-field phasors	39
5.4 Numerical results	41
5.5 Closing remarks	49
5.6 Extension problem — Different positions of the dipole source inside an infil- trated CSTF	51
5.6.1 Numerical results and comparison with previous results	51
5.6.2 Concluding remarks	54
6 Columnar thin film as platforms for surface-plasmonic-polaritonic optical sens- ing	56
6.1 Introduction	56
6.2 Constitutive parameters of an infiltrated CTF	57
6.3 Canonical boundary-value problem	60

6.4	Modified Kretschmann configuration	63
6.5	Closing remarks	68
7	Chiral sculptured thin film as dual-functioning optical sensors	70
7.1	Introduction	70
7.2	Constitutive parameters of an infiltrated CSTF	71
7.3	Boundary-value problem	73
7.4	Numerical results	74
7.4.1	Surface multiplasmonics	75
7.4.2	Circular Bragg phenomenon	79
7.5	Closing remarks	81
8	Conclusions and further research	83
A	The Bruggeman formalism for inverse homogenization	85
B	Surface plasmon polariton waves	87
B.1	Introduction	87
B.2	Brief theory of surface plasmon polaritons	87
B.3	Excitation of SPPs	90
B.4	Conclusions	91
C	Extension problem — Different positions of the dipole source inside an infiltrated CSTF	92
	Bibliography	107

List of Acronyms and Symbols

Acronyms

CBP	circular Bragg phenomenon
CLC	cholesteric liquid crystal
CSTF	chiral sculptured thin film
CTF	columnar thin film
LCP	left circular polarization
RCP	right circular polarization
SMP	surface multiplasmonics
SPFT	strong-permittivity-fluctuation theory
SPP	surface-plasmonic-polaritonic
STF	sculptured thin film

Operators and functions

$\underline{\underline{A}}^{adj}$	adjoint of matrix A
$\underline{\underline{A}}^{-1}$	inverse of matrix A
$\underline{\underline{A}}^T$	transpose of matrix A
$\det[\underline{\underline{A}}]$	determinant of matrix A
$\text{Im}\{\cdot\}$	imaginary part of
$\text{Re}\{\cdot\}$	real part of
$\text{tr}[\underline{\underline{A}}]$	trace of matrix A
$\delta(\cdot)$	Dirac delta function

Scalar

f	volume fraction
k_0	free-space wavenumber
L	correlation length
n_ℓ	refractive index of the fluid filling the void region
n_s	refractive index of the deposited material
r_p	complex-valued reflection
r_t	complex-valued transmission
Z_0	free-space intrinsic impedance
ϵ_0	permittivity of free-space
μ_0	permeability of free-space
λ_0	free-space wavelength
χ	column inclination angle
χ_v	vapour flux incidence angle
η	size parameter
γ_b	shape parameter
ω	angular frequency
ϵ_m	permittivity of metal
θ_{inc}	angle of incidence

Vectors

B	magnetic induction
D	dielectric displacement
E	electric field
H	magnetic field
J	source density
$\hat{\mathbf{r}}$	position vector
$\mathbf{u}_{x,y,z}$	cartesian unit vectors
$\mathbf{u}_{\tau,n,b}$	tangential, normal and binormal unit vectors

3×3 dyadics

$\underline{\underline{a}}$	polarizability dyadic
$\underline{\underline{D}}$	depolarization dyadic
$\underline{\underline{I}}$	identity dyadic
$\underline{\underline{G}}$	dyadic Green function
$\underline{\underline{U}}$	shape dyadic
$\underline{\underline{S}}_{x,y,z}$	rotational dyadics
$\underline{\underline{\epsilon}}_{cstf}$	permittivity constitutive dyadic of CSTF
$\underline{\underline{\epsilon}}_{ctf}$	permittivity constitutive dyadic of CTF
$\underline{\underline{\Sigma}}^{[n]}$	n th-order mass operator

List of Figures

1.1	Framework of research	4
2.1	Schematic image of the component particles for the Maxwell Garnett formalism. All the ellipsoidal particles have the same shape and orientation, but randomly distributed. (Image is reprinted from [16]).	12
2.2	Schematic image of the component particles for the Bruggeman formalism. All material a and material b particles have the same ellipsoidal shape, but the shape for each component materials are generally different. The particles for each component materials are randomly distributed but have identical orientation. (Image is reprinted from [16]).	12
2.3	Schematic image of the component particles for the SPFT. All material a and material b particles have the same ellipsoidal shape. The particles for each component material are randomly distributed, but have identical orientation. (Image is reprinted from [16]).	14
3.1	Plots of ϵ_a as determined by the inverse Bruggeman formalism (red, solid curves) and the inverse Maxwell Garnett formalism (blue, dashed curves) versus f_a for $\epsilon_b = \pm 2$ and $\epsilon_{hcm}^{Br,MG} = 3$. Estimates of ϵ_a delivered by the inverse Maxwell Garnett formalism are strictly valid only for $f_a \lesssim 0.3$	19
3.2	Plots of the real and imaginary parts of ϵ_a as determined by the inverse Brugge- man formalism (red, solid curves) and the inverse Maxwell Garnett formal- ism (blue, dashed curves) versus f_a for $\epsilon_b = 2$ and $\epsilon_{hcm}^{Br,MG} = 3 + \delta i$ where $\delta \in \{0.1, 1, 10\}$. Estimates of ϵ_a delivered by the inverse Maxwell Garnett for- malism are strictly valid only for $f_a \lesssim 0.3$	20
3.3	As Fig. 3.2 except that $\epsilon_b = -2$	21
4.1	Scanning electron micrograph of CTE (Image is reprinted from [44])	24

4.2	Scanning electron micrograph of CSTF. (Image is reprinted from [49])	25
4.3	Schematic of (a) CTF and (b) CSTF growing, with column inclination angle χ , on a substrate. The vapour incidence angle is $\chi_v \leq \chi$. The columns grow along the direction of the unit vector \mathbf{u}_τ	27
5.1	Real and imaginary parts of the relative permittivity parameters ϵ_{a2} , ϵ_{b2} and ϵ_{c2} versus refractive index $n_\ell \in (1, 1.5)$ and relative size parameter $k_0\eta \in (0, 0.2)$	35
5.2	A schematic diagram of the scenario under investigation: radiation emitted from a dipole source embedded within an infiltrated CSTF occupying $-L < z < L$. Herein, CSTF is made from patinal [®] titanium oxide.	36
5.3	Projections of $ \mathbf{P}_{LCP} $ and $ \mathbf{P}_{RCP} $ (scaled by $10^{13}\omega^{-2} p ^{-2}$) onto the $z = 0$ plane for $z^{obs} > L$ and $z^{obs} < -L$. Here $\lambda_0 \in \{683.6\text{nm}, 763.6\text{nm}, 803.6\text{nm}\}$ and $n_\ell = 1.0$	43
5.4	As Fig. 5.3 but with $\lambda_0 \in \{745.2\text{nm}, 825.2\text{nm}, 865.2\text{nm}\}$ and $n_\ell = 1.25$. The relative permittivity parameters $\{\epsilon_{a2}, \epsilon_{b2}, \epsilon_{c2}\}$ for the infiltrated CSTF were computed using the non-extended version of the Bruggeman homogenization formalism.	44
5.5	As Fig. 5.4 but with $\lambda_0 \in \{804.9\text{nm}, 884.9\text{nm}, 924.9\text{nm}\}$ and $n_\ell = 1.5$	45
5.6	λ_0^{Br} and $\Delta\lambda_0^{Br}$ plotted against n_ℓ for $\theta^{obs} = 0^\circ$ (solid, red curve), $\theta^{obs} = 30^\circ$ (dashed, green curve) and $\theta^{obs} = 60^\circ$ (broken dashed, blue curve). The relative permittivity parameters $\{\epsilon_{a2}, \epsilon_{b2}, \epsilon_{c2}\}$ for the infiltrated CSTF were computed using the non-extended version of the Bruggeman homogenization formalism.	46
5.7	As Fig. 5.3 but the relative permittivity parameters $\{\epsilon_{a2}, \epsilon_{b2}, \epsilon_{c2}\}$ for the infiltrated CSTF were computed using the extended version of the Bruggeman homogenization formalism with $\eta = 0.1/k_0$, and $\lambda_0 \in \{688.4\text{nm}, 768.4\text{nm}, 808.4\text{nm}\}$	47
5.8	As Fig. 5.7 but with $\lambda_0 \in \{746.5\text{nm}, 826.5\text{nm}, 866.5\text{nm}\}$	48
5.9	As Fig. 5.7 but with $\lambda_0 \in \{810.1\text{nm}, 890.1\text{nm}, 930.1\text{nm}\}$	49
5.10	λ_0^{Br} and $\Delta\lambda_0^{Br}$ plotted against $k_0\eta$ for $n_\ell = 1.0$ (solid, red curve), $n_\ell = 1.25$ (dashed, green curve) and $n_\ell = 1.5$ (broken dashed, blue curve), as computed using the extended Bruggeman homogenization formalism. The angle $\theta^{obs} = 0^\circ$	50
5.11	The projections of \mathbf{P}_{LCP} and \mathbf{P}_{RCP} with $\epsilon_{a2} = 4.6$, $\epsilon_{b2} = 5.4$, $\epsilon_{c2} = 5.0$ and $n_\ell = 1.5$ which were computed using non-extended version of the Bruggeman homogenization formalism and $z > L$ is filled by a fluid of refractive index $n_\ell = 1.5$	52

5.12	The projections of \mathbf{P}_{RCP} with $\epsilon_{a2} = 4.6$, $\epsilon_{b2} = 5.4$, $\epsilon_{c2} = 5.0$ and $n_\ell = 1.5$. Also (a) $z = L - 40$, (b) $z = L - 40 - 1200$, (c) $z = L - 40 - 2400$, (d) $z = L - 40 - 3600$, (e) $z = L - 40 - 4800$ and (f) $z = L - 40 - 6000$ and $z > L$ is filled by a fluid of refractive index $n_\ell = 1.5$	53
5.13	The projections of \mathbf{P}_{RCP} with $\epsilon_{a2} = 4.6$, $\epsilon_{b2} = 5.4$, $\epsilon_{c2} = 5.0$ and $n_\ell = 1.5$. Also (a) $z = L - 40$, (b) $z = L - 40 - 1200$, (c) $z = L - 40 - 2400$, (d) $z = L - 40 - 3600$, (e) $z = L - 40 - 4800$ and (f) $z = L - 40 - 6000$ and there is no fluid above the CSTF.	53
5.14	The projections of \mathbf{P}_{RCP} with $\epsilon_{a2} = 4.6$, $\epsilon_{b2} = 5.4$, $\epsilon_{c2} = 5.0$ and $n_\ell = 1.5$. Also (a) $z = L/2 + 200$, (b) $z = L/2 + 160$, (c) $z = L/2 + 120$, (d) $z = L/2 + 80$, (e) $z = L/2 + 40$, (f) $z = L/2$, (g) $z = L/2 - 40$, (h) $z = L/2 - 80$, (i) $z = L/2 - 120$, (j) $z = L/2 - 160$ and (k) $z = L/2 - 200$ and there is no fluid above the CSTF.	55
6.1	The real and imaginary parts of the relative permittivity parameter ϵ_{a2} of a fluid-infiltrated CTF, as computed using the extended second-order SPFT, plotted against $\eta/L \in (0, 1)$ and $k_0L \in (0, 0.2)$. The refractive index of the fluid infiltrating the CTF is fixed at $n_\ell = 1.5$	61
6.2	The real and imaginary parts of the relative wavenumber σ plotted against $\eta/L \in (0, 1)$ and $k_0L \in (0, 0.2)$	62
6.3	The real part of q_c plotted against $\eta/L \in (0, 1)$ and $k_0L \in (0, 0.2)$	62
6.4	A p -polarized plane wave incident on a metal-coated, infiltrated CTF in the modified Kretschmann configuration. The incident electric field phasor \mathbf{E}_{inc} ($z < 0$) gives rise to a reflected electric field phasor \mathbf{E}_{ref} ($z < 0$) and a transmitted electric field phasor \mathbf{E}_{tr} ($z > L_\Sigma$).	63
6.5	The absorbance A_p (red, solid curve) plotted against θ_{inc} (in degree), for the modified Kretschmann configuration with $\epsilon_d = 6.76$, $\epsilon_m = -56 + 21i$, $\epsilon_\ell = 2.25$, $L_m = 10$ nm, $L_\Sigma = L_m + 1000$ nm, $\eta/L = 1.0$ and $k_0L = 0.2$. Also plotted is the quantity $ r_p ^2$ (blue, dashed curve), calculated when $L_m = 0$. Here, $\theta_{inc}^\# = 70.8^\circ$	65
6.6	As Fig. 6.5 except that the quantities plotted are the reflectance $ r_p ^2$ (red, solid curve) and $\beta t_p ^2$ (blue, dashed curve). Here, $\theta_{inc}^\# = 70.8^\circ$	65
6.7	The angle $\theta_{inc}^\#$ (in degree) for the scenario represented in Fig. 6.6, plotted versus $\eta/L \in (0, 1)$ and $k_0L \in (0, 0.2)$	66
6.8	As Fig. 6.7 except that the quantity plotted is $d^2(r_p ^2)/d\theta_{inc}^2$ (in per degree ²), evaluated at $\theta_{inc} = \theta_{inc}^\#$	66

6.9	The figure of merit ρ (in degree/RIU) plotted against $\eta/L \in (0, 1)$ and $k_0 L \in (0, 0.2)$ for $n_{\ell 2} = 1.5$ and $n_{\ell 1} = 1.0$	67
6.10	The dynamic figure of merit ρ_{RI} (in degree/RIU) plotted against $\eta/L \in (0, 1)$ and $k_0 L \in (0, 0.2)$ for $n_{\ell} = 1.5$	68
7.1	A schematic diagram of the geometry under consideration.	72
7.2	Absorptance for incident LCP (red, solid curve) and RCP (blue, dashed curve) plane waves plotted versus θ_{inc} for $n_l = 1.25$, $\chi_v = 25^\circ$, and $\lambda_0 = 526.4$ nm. . . .	75
7.3	As Fig. 7.2 except that the quantities plotted are the reflectances $R_L = R_{LL} + R_{RL}$ (red, solid curve) and $R_R = R_{LR} + R_{RR}$ (blue, dashed curve).	76
7.4	Angles $\tilde{\theta}_{inc}^{(1)}$ and $\tilde{\theta}_{inc}^{(2)}$ plotted against the refractive index n_l and free-space wavelength λ_0 , for $\chi_v = 25^\circ$. The acronym RIU stands for <i>refractive-index unit</i>	77
7.5	Sharpness of R_R peak, as gauged by the second derivative $d^2 R_R / d\theta_{inc}^2$ evaluated at $\theta_{inc} = \tilde{\theta}_{inc}^{(1)}$ and $\tilde{\theta}_{inc}^{(2)}$, against the refractive index n_l and free-space wavelength λ_0 , for $\chi_v = 25^\circ$	77
7.6	Figures of merit $\rho^{(1)}$ and $\rho^{(2)}$ plotted against the refractive index n_l and free-space wavelength λ_0 , for $\chi_v = 25^\circ$	78
7.7	Refractive-index sensitivity $\rho_{RI}^{(1)}$ and $\rho_{RI}^{(2)}$ plotted against the refractive index n_l and free-space wavelength λ_0 , for $\chi_v = 25^\circ$	78
7.8	Reflectances $R_{LL,LR,RL,RR}$ and transmittances $T_{LL,LR,RL,RR}$ plotted against the free-space wavelength λ_0 for $\chi_v = 25^\circ$ and $\theta_{inc} = 10^\circ$. The CSTF is infiltrated with a fluid of refractive index $n_l = 1.0$ (blue, broken-dashed curves), 1.25 (red, solid curves) and 1.5 (green, dashed curves).	80
7.9	As for the R_{RR} plots in Fig. 7.8 except (a) for $\chi_v = 15^\circ$ and (b) for $\chi_v = 30^\circ$	81
7.10	Refractive-index sensitivity $d\lambda_0^{hole} / dn_l$ plotted against λ_0^{hole} for $\chi_v = 15^\circ$ (blue, broken dashed curve), 25° (red, thick solid curve), and 30° (green, dashed curve). . . .	81
A.1	Plots of the real and imaginary parts of ϵ_a as determined by the inverse Bruggeman formalism (red, solid curves) and the inverse Maxwell Garnett formalism (blue, dashed curves) versus f_a for $\epsilon_b = 2$ and $\epsilon_{hcm}^{Br,MG} = 3 + \delta i$ where $\delta \in \{0.01, 0.001\}$	85
A.2	Plots of the real and imaginary parts of ϵ_a as determined by the inverse Bruggeman formalism (red, solid curves) and the inverse Maxwell Garnett formalism (blue, dashed curves) versus f_a for $\epsilon_b = -2$ and $\epsilon_{hcm}^{Br,MG} = 3 + \delta i$ where $\delta \in \{0.01, 0.001\}$	86

B.1	Schematic for SPP propagation at interface between metal and dielectric material.	88
B.2	Distribution for the electric field of a p -polarized SPP wave at interface between metal and dielectric material.	89
C.1	The projections of P_{LCP} and P_{RCP} with $\epsilon_{a2} = 3.26$, $\epsilon_{b2} = 4.46$, $\epsilon_{c2} = 3.78$ and $n_l = 1.0$ which were computed using non-extended version of the Bruggeman homogenization formalism and there is no fluid above the CSTF.	93
C.2	The projections of P_{LCP} and P_{RCP} with $\epsilon_{a2} = 3.89$, $\epsilon_{b2} = 4.9$, $\epsilon_{c2} = 4.4$ and $n_l = 1.25$ which were computed using non-extended version of the Bruggeman homogenization formalism and there is no fluid above the CSTF.	94
C.3	The projections of P_{LCP} and P_{RCP} with $\epsilon_{a2} = 3.89$, $\epsilon_{b2} = 4.9$, $\epsilon_{c2} = 4.4$ and $n_l = 1.25$ which were computed using non-extended version of the Bruggeman homogenization formalism and $z > L$ is filled by a fluid of refractive index $n_\ell = 1.5$	95
C.4	The projections of P_{LCP} and P_{RCP} with $\epsilon_{a2} = 3.94 + 0.0075i$, $\epsilon_{b2} = 4.92 + 0.0085i$, $\epsilon_{c2} = 4.38 + 0.0084i$ and $n_l = 1.25$ which were computed using extended version of the Bruggeman homogenization formalism and $z > L$ is filled by a fluid of refractive index $n_\ell = 1.5$	96
C.5	The projections of P_{LCP} and P_{RCP} with $\epsilon_{a2} = 4.6$, $\epsilon_{b2} = 5.4$, $\epsilon_{c2} = 5.0$ and $n_l = 1.5$ which were computed using non-extended version of the Bruggeman homogenization formalism and there is no fluid above the CSTF.	97

Chapter 1

Introduction

1.1 Background of Research

Composite materials are produced by mixing together different component materials. This process has been studied for quite a long time ago, and has been applied in various applications. A mixture of materials may be considered effectively homogenous when wavelengths are much larger than the particle sizes of the component materials. The estimation of the constitutive parameters of such a homogenized composite material (HCM) is central to the work described in this thesis. Several theoretical approaches can be implemented to estimate the constitutive parameters of HCM [1, 2, 3]. The most common approaches are based on the Maxwell Garnett formalism and the Bruggeman formalism [4]. Like most conventional approaches to homogenization, the Maxwell Garnett formalism and the Bruggeman formalism do not take the statistical distribution of the component particles into account. Instead, the spatial distributions are characterized by volume fraction alone. Moreover, the depolarization dyadics which characterize the electromagnetic response of each component particle embedded in the comparison medium is treated on a vanishingly small region and is represented by the singularity of the corresponding dyadic Green function [5, 6]. In this thesis the conventional homogenization formalisms were used Chap. 3 (Maxwell Garnett and Bruggeman) and Chap. 7 (Bruggeman). In Chap. 5 the extended homogenization formalism based on Bruggeman formalism which takes into account the size of the component particles is used. Meanwhile, in Chap. 6 the statistical distribution of the components phases is taken into account in a more sophisticated homogenization approach known as strong-property-fluctuation theory (SPFT) [7, 8, 9]. This approach is also known as strong-permittivity-fluctuation theory when it is applied to dielectric materials.

1.2 Objectives of Research

The aims of this project are as follows;

- a) to understand the concept of homogenization formalisms and including inverse homogenization
- b) to study sculptured thin films (STFs), especially columnar thin films (CTFs) and chiral sculptured thin films (CSTFs), with a view to possible applications as optical sensors
- c) to explore the emission of electromagnetic radiation from a dipole source embedded inside an infiltrated CSTF where the extended version of Bruggeman formalism is implemented in homogenization studies
- d) to investigate the potential of CTF as platforms for exciting surface plasmon polariton (SPP) where the extended version of the second order SPFT is employed in homogenization studies
- e) to elucidate the ability of CSTF for exciting surface multi plasmonic (SMP) and exploiting circular Bragg phenomenon (CBP) in parallel where the non-extended version of Bruggeman formalism is applied in homogenization studies

1.3 Importance of Research

The work in this thesis is chiefly aimed at providing a guideline for experimental efforts by presenting numerical studies. We predict how the design parameters of an infiltrated STF which accommodates a more sophisticated homogenization formalisms effect its performance and sensitivity based on optical sensors in particular in exciting SPP and exploiting CBP.

1.4 Framework of Research

This thesis consists of eight chapters. The first chapter discusses the background of research, objectives of research, importance of research and framework of research.

In Chap. 2, the theory describing the electromagnetic response of an inclusion embedded in the comparison medium and the statistical distribution of the components phases is

presented. This chapter also provides discussion on conventional approaches of homogenization to estimate the constitutive parameters of HCMs, namely Maxwell Garnet formalism, Bruggeman formalism and SPFT.

Chap. 3 is focused on the Bruggeman formalism for inverse homogenization. The limitation of this formalism is studied by comparing the results with the inverse Maxwell Garnett formalism. Numerical studies are presented for dissipative and nondissipative homogenization scenarios.

The background of STF is provided in Chap. 4. Two types of STF are considered, i.e., CTF and CSTF. Homogenization studies on these STF used to estimate their constitutive parameters also presented in this chapter.

In Chap. 5, the emission of electromagnetic radiation from a dipole source embedded inside an infiltrated CSTF is explored. The extended version of Bruggeman formalism is implemented. This study is extended by investigating the influence of different positions of the dipole source. The non-extended version of the Bruggeman formalism is considered in this case.

Chap. 6 is investigating the potential of CTF as platforms for exciting SPP. Higher order homogenization technique, based on an extended version of the second order SPFT is used to estimate the constitutive parameters of the infiltrated CTF.

Our final numerical works are revealed in Chap. 7. This work investigates the ability of CSTF for exciting SMP and exploiting CBP in parallel. In order to determine the relative permittivity parameters of the infiltrated CSTF, the non-extended version of Bruggeman homogenization formalism is implemented.

Chap. 8 consists the summary of this research. Also provided are some recommendations for future works. The framework of this research is summarized in Fig. 1.1.

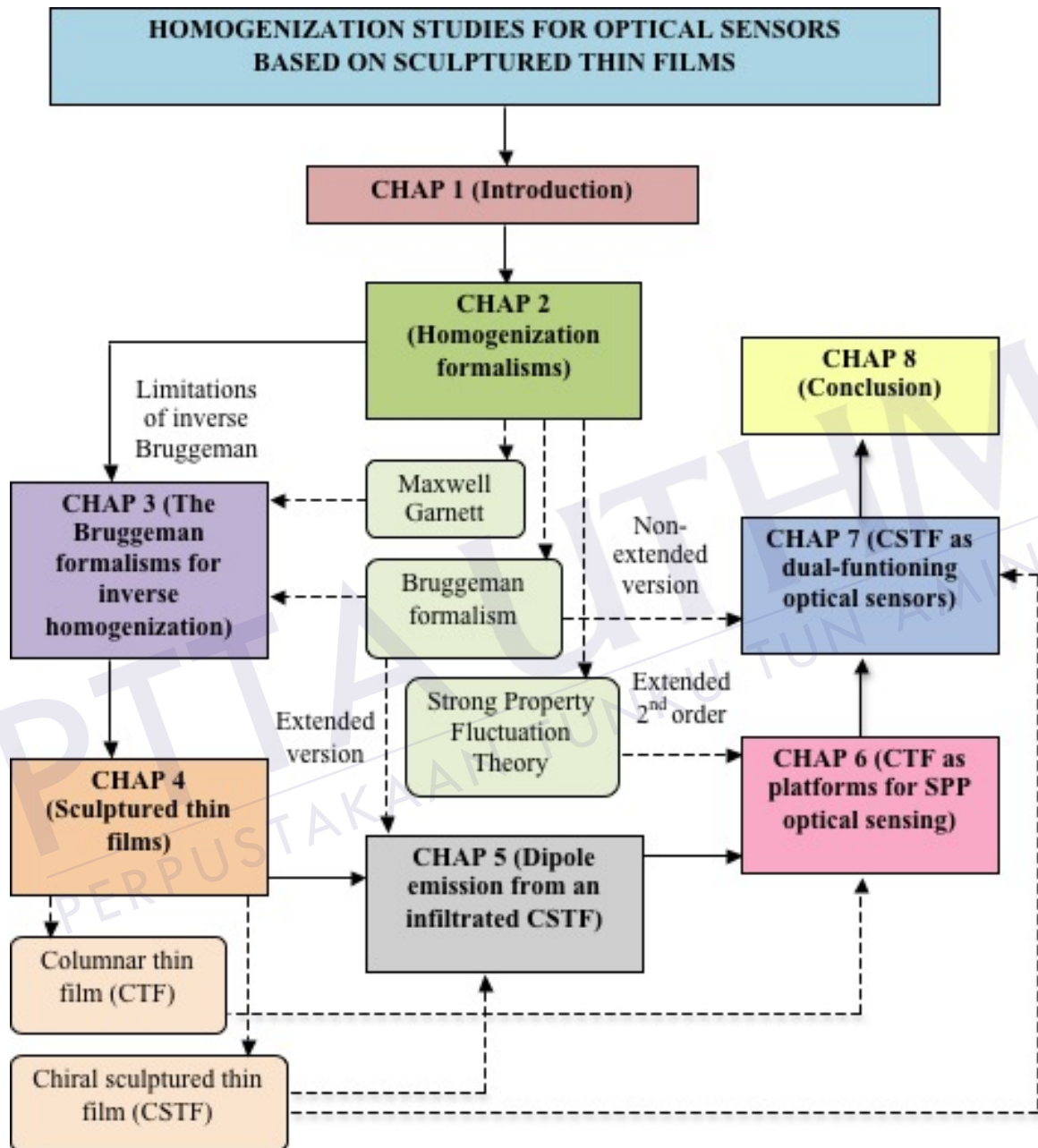


Figure 1.1: Framework of research

Chapter 2

Homogenization formalisms

2.1 Introduction

The mixture of two component materials yields a composite material which may be regarded as effectively homogeneous when the particle sizes of the component material are small enough compared to wavelengths involved. The estimation study of the effective constitutive parameters of such homogenized composite materials (HCMs) is the main focus in this chapter. In order to achieve this, we first provide a brief introduction to Maxwell equations [10] and constitutive relations which is important in describing the electromagnetic properties of the materials, as provided in Sec. 2.2. It is followed by a presentation of the theory of the depolarization dyadic (Sec. 2.3) and distributional statistics (Sec. 2.4) which both provide the nanostructural details of the ellipsoidal particles inside the materials. Finally, the homogenization formalisms studies are given in Sec. 2.5. We considered three homogenization formalisms i.e., Maxwell Garnett formalism, Bruggeman formalism and strong-property-fluctuation theory (SPFT).

2.2 The Maxwell Equations and Constitutive Relations

The Maxwell equations provide the starting point in characterizing all electromagnetic phenomena. Maxwell equations in the time-domain take the form [11]

$$\nabla \times \tilde{\mathbf{E}}(\mathbf{r}, t) = -\frac{\partial}{\partial t} \tilde{\mathbf{B}}(\mathbf{r}, t), \quad (2.1)$$

$$\nabla \times \tilde{\mathbf{H}}(\mathbf{r}, t) = \frac{\partial}{\partial t} \tilde{\mathbf{D}}(\mathbf{r}, t) + \tilde{\mathbf{J}}(\mathbf{r}, t), \quad (2.2)$$

$$\nabla \cdot \tilde{\mathbf{B}}(\mathbf{r}, t) = 0, \quad (2.3)$$

$$\nabla \cdot \tilde{\mathbf{D}}(\mathbf{r}, t) = \tilde{\rho}(\mathbf{r}, t), \quad (2.4)$$

where $\tilde{\mathbf{E}}(\mathbf{r}, t)$, $\tilde{\mathbf{H}}(\mathbf{r}, t)$, $\tilde{\mathbf{D}}(\mathbf{r}, t)$ and $\tilde{\mathbf{B}}(\mathbf{r}, t)$ stand for the electric field, magnetic field, dielectric displacement and magnetic induction respectively, while the current and charge densities are represented by $\tilde{\mathbf{J}}(\mathbf{r}, t)$ and $\tilde{\rho}(\mathbf{r}, t)$, respectively. In the following, we only make use of 2.1 and 2.2. Eqs. 2.3 and 2.4 can be derived from 2.1 and 2.2 under the assumption of continuity of charge [11]. The two vector differential equation 2.1 and 2.2 involve four unknown vector fields, $\tilde{\mathbf{E}}(\mathbf{r}, t)$, $\tilde{\mathbf{H}}(\mathbf{r}, t)$, $\tilde{\mathbf{D}}(\mathbf{r}, t)$ and $\tilde{\mathbf{B}}(\mathbf{r}, t)$. In order to allow a unique solution for the field vectors, further equations are required. These equations take the form of the constitutive relations which characterize the behaviour of the material when applying fields to the material. For an anisotropic dielectric medium, the constitutive relations may be written as [11, 12]

$$\tilde{\mathbf{D}}(\mathbf{r}, t) = \int_{-\infty}^0 \underline{\underline{\tilde{\epsilon}}}(\mathbf{r}, t') \cdot \tilde{\mathbf{E}}(\mathbf{r}, t - t') dt', \quad (2.5)$$

$$\tilde{\mathbf{B}}(\mathbf{r}, t) = \mu_0 \tilde{\mathbf{H}}(\mathbf{r}, t), \quad (2.6)$$

where $\underline{\underline{\tilde{\epsilon}}}(\mathbf{r}, t')$ indicates the time domain permittivity dyadic, while μ_0 represents the permeability of free space which both have a role in specifying the material. The time dependence of $\tilde{\mathbf{D}}$ is different to that of $\tilde{\mathbf{E}}$ since the material requires some time to respond to the applied field.

In solving for fields $\tilde{\mathbf{D}}$ and $\tilde{\mathbf{E}}$, it is complicated if the constitutive relations 2.5 and 2.6 are directly substituted into the Maxwell equations 2.1 and 2.2. Instead, we introduce Fourier transformation [13]

$$\mathbf{f}(\mathbf{r}, \omega) = \frac{1}{2\pi} \int_{-\infty}^{\infty} \tilde{\mathbf{f}}(\mathbf{r}, t) \exp(i\omega t) dt, \quad (2.7)$$

to transfer the time-domain to the frequency-domain. The $\mathbf{f}(\mathbf{r}, \omega)$ is representing the frequency-domain $\underline{\underline{\epsilon}}_r$, \mathbf{E} , \mathbf{D} , \mathbf{B} , \mathbf{H} and \mathbf{J} while ω is an angular frequency.

After applying Fourier transform to 2.5 and 2.6 along with the convolution theorem[13] Suppose that $f(\mathbf{r}, t)$ and $g(\mathbf{r}, t)$ are piecewise continuous, bounded, and absolutely integrable on the t -axis. Then the convolution is

$$(f * g)(\mathbf{r}, t) = \int_{-\infty}^{+\infty} f(\mathbf{r}, t') g(\mathbf{r}, t - t') dt', \quad (2.8)$$

and its Fourier transformation

$$\mathcal{F}(f * g) = \sqrt{2\pi} \mathcal{F}(f) \mathcal{F}(g), \quad (2.9)$$

the constitutive relations in frequency-domain may be written as

$$\mathbf{D}(\mathbf{r}, \omega) = \underline{\underline{\epsilon}}(\mathbf{r}, \omega) \cdot \mathbf{E}(\mathbf{r}, \omega), \quad (2.10)$$

$$\mathbf{B}(\mathbf{r}, \omega) = \mu_0 \mathbf{H}(\mathbf{r}, \omega). \quad (2.11)$$

Therefore, the Maxwell equations 2.1 and 2.2 are presented in the frequency-domain as

$$\nabla \times \mathbf{E}(\mathbf{r}, \omega) = i\omega\mu_0 \mathbf{H}(\mathbf{r}, \omega), \quad (2.12)$$

$$\nabla \times \mathbf{H}(\mathbf{r}, \omega) = -i\omega \underline{\underline{\epsilon}}(\mathbf{r}, \omega) \cdot \mathbf{E}(\mathbf{r}, \omega) + \mathbf{J}(\mathbf{r}, \omega). \quad (2.13)$$

Upon eliminating $\mathbf{H}(\mathbf{r}, \omega)$ from 2.12 and 2.13, we obtain

$$\nabla \times \nabla \times \mathbf{E}(\mathbf{r}, \omega) - \omega^2 \mu_0 \underline{\underline{\epsilon}}(\mathbf{r}, \omega) \cdot \mathbf{E}(\mathbf{r}, \omega) = i\omega\mu_0 \mathbf{J}(\mathbf{r}, \omega). \quad (2.14)$$

Since 2.14 is a linear equation, we may express its solution in terms of dyadic Green function per

$$\mathbf{E}(\mathbf{r}, \omega) = i\omega\mu_0 \int_V \underline{\underline{G}}(\mathbf{r} - \mathbf{r}', \omega) \cdot \mathbf{J}(\mathbf{r}', \omega) d^3\mathbf{r}'. \quad (2.15)$$

Herein, $\underline{\underline{G}}(\mathbf{r} - \mathbf{r}', \omega)$ is called the dyadic Green function which is a function of the field point \mathbf{r} and the source point \mathbf{r}' . The integration is calculated within the source region V . Substitution of 2.15 into 2.14 shows that $\underline{\underline{G}}(\mathbf{r} - \mathbf{r}', \omega)$ must satisfies the differential equation [11]

$$\nabla \times \nabla \times \underline{\underline{G}}(\mathbf{r} - \mathbf{r}', \omega) - \omega^2 \mu_0 \underline{\underline{\epsilon}}(\mathbf{r}, \omega) \cdot \underline{\underline{G}}(\mathbf{r} - \mathbf{r}', \omega) = \delta(\mathbf{r} - \mathbf{r}') \underline{\underline{I}}, \quad (2.16)$$

with $\delta(\mathbf{r} - \mathbf{r}')$ is the Dirac delta function and $\underline{\underline{I}}$ is 3×3 identity dyadic representing the source terms in 2.14. Generally, the dyadic Green function can be thought as representing the response of the medium at \mathbf{r} to a point source at \mathbf{r}' .

2.3 Depolarization dyadic

Depolarization dyadics play an important role in characterizing the electromagnetic response of an ellipsoidal inclusion embedded in an anisotropic dielectric comparison medium, for example, which take the form [14]

$$\underline{\underline{D}}_{cm} = \int_{V_e^\eta} \underline{\underline{G}}_{cm}(\mathbf{r}) d^3\mathbf{r} = \int_{V^\eta} \underline{\underline{G}}_{cm}(\underline{\underline{U}} \cdot \mathbf{r}) d^3\mathbf{r}. \quad (2.17)$$

Herein, $\underline{\underline{G}}_{cm}$ is the dyadic Green function of the comparison medium in which the inclusion is embedded. Explicit expressions for dyadic Green functions are not generally available for anisotropic materials. However, it suffices here to consider the spatial Fourier transform of $\underline{\underline{G}}_{cm}(\mathbf{r})$, viz

$$\tilde{\underline{\underline{G}}}_{cm}(\mathbf{q}) = \int_{\mathbf{r}} \underline{\underline{G}}_{cm}(\mathbf{r}) \exp(i\mathbf{q} \cdot \mathbf{r}) d^3\mathbf{r}, \quad (2.18)$$

and which can be found by taking the spatial Fourier transform of 2.16. We obtain

$$\tilde{\underline{\underline{G}}}_{cm}(\mathbf{q}) = -i\omega\mu_0 \left(\mathbf{q} \times \mathbf{q} \times \underline{\underline{I}} + \omega^2 \mu_0 \underline{\underline{\epsilon}}_{cm} \right)^{-1}, \quad (2.19)$$

wherein $\underline{\underline{\epsilon}}_{cm}$ denotes the permittivity dyadic of the comparison medium. The ellipsoidal surface of V_e^η in 2.17 is parametrized by

$$\mathbf{r}_e(\theta, \phi) = \eta \underline{\underline{U}} \cdot \hat{\mathbf{r}}(\theta, \phi), \quad (2.20)$$

in which $\hat{\mathbf{r}}(\theta, \phi)$ is the radial unit vector specified by the spherical polar coordinates θ and ϕ . The symmetric shape dyadic $\underline{\underline{U}}$ (of unit determinant) maps the spherical region V^η of radius η onto the ellipsoidal region V_e^η . The dyadic Green function in the case of an anisotropic dielectric comparison medium [5], characterized by the permittivity dyadic $\underline{\underline{\epsilon}}_{cm}$, satisfies the partial differential equation 2.16. In order to consider the depolarization of an inclusion of nonzero volume, $\underline{\underline{D}}$ is expressed as the sum [14]

$$\underline{\underline{D}}_{U/cm}(\eta) = \underline{\underline{D}}_{U/cm}^0 + \underline{\underline{D}}_{U/cm}^\eta(\eta), \quad (2.21)$$

where

$$\underline{\underline{D}}_{U/cm}^0 = \lim_{\eta \rightarrow 0} \frac{\eta}{2\pi^2} \int_{\mathbf{q}} \frac{1}{q^2} \left(\frac{\sin(q\eta)}{q\eta} - \cos(q\eta) \right) \tilde{\underline{\underline{G}}}_{cm}^\infty(\underline{\underline{U}}^{-1} \cdot \mathbf{q}) d^3\mathbf{q}, \quad (2.22)$$

$$\underline{\underline{D}}_{U/cm}^\eta(\eta) = \frac{\eta}{2\pi^2} \int_{\mathbf{q}} \frac{1}{q^2} \left(\frac{\sin(q\eta)}{q\eta} - \cos(q\eta) \right) \tilde{\underline{\underline{G}}}_{cm}^\eta(\underline{\underline{U}}^{-1} \cdot \mathbf{q}) d^3\mathbf{q}, \quad (2.23)$$

and

$$\tilde{G}_{\underline{\underline{cm}}}^{\infty}(\underline{U}^{-1} \cdot \underline{\mathbf{q}}) = \lim_{q \rightarrow \infty} \tilde{G}_{\underline{\underline{cm}}}(\underline{U}^{-1} \cdot \underline{\mathbf{q}}), \quad (2.24)$$

$$\tilde{G}_{\underline{\underline{cm}}}^{\eta}(\underline{U}^{-1} \cdot \underline{\mathbf{q}}) = \tilde{G}_{\underline{\underline{cm}}}(\underline{U}^{-1} \cdot \underline{\mathbf{q}}) - \tilde{G}_{\underline{\underline{cm}}}^{\infty}(\underline{U}^{-1} \cdot \underline{\mathbf{q}}). \quad (2.25)$$

Thus, the dyadic $\underline{D}_{\underline{\underline{U/cm}}}^0$ corresponds to the limit $\eta \rightarrow 0$ i.e., considering vanishingly small inclusions, whereas the dyadic $\underline{D}_{\underline{\underline{U/cm}}}^{\eta}$ provides the nonzero size of the inclusion particles i.e., $k_0\eta \ll 1$ but $k_0\eta > 0$ where k_0 is wavenumber in free space and $k_0 = 2\pi/\lambda$ with λ being wavelength. The volume integral 2.22 can be simplified to the η -independent double integral [5, 6]

$$\underline{D}_{\underline{\underline{U/cm}}}^0 = \frac{1}{4\pi i \omega} \int_0^{2\pi} d\phi \int_0^{\pi} d\theta \sin\theta \left(\frac{1}{\text{tr}(\underline{\epsilon}_{\underline{\underline{cm}}} \cdot \underline{A})} \underline{A} \right), \quad (2.26)$$

where

$$\underline{A} = \text{diag} \left(\frac{\sin^2 \theta \cos^2 \phi}{U_x^2}, \frac{\sin^2 \theta \sin^2 \phi}{U_y^2}, \frac{\cos^2 \theta}{U_z^2} \right) \quad (2.27)$$

$$\text{for } \underline{U} = \begin{pmatrix} U_x & 0 & 0 \\ 0 & U_y & 0 \\ 0 & 0 & U_z \end{pmatrix}.$$

On the other hand, by applying the residue calculus to 2.23, we have the surface integral

$$\underline{D}_{\underline{\underline{U/cm}}}^{\eta}(\eta) = \frac{1}{4\pi i \omega} \eta^3 \int_0^{2\pi} d\phi \int_0^{\pi} d\theta \frac{\sin\theta}{3\Delta} \left\{ \left[\frac{3(\kappa_+ - \kappa_-)}{2\eta} + i(\kappa_+^{3/2} - \kappa_-^{3/2}) \right] \underline{\alpha} + i\omega^2 \mu_0 (\kappa_+^{1/2} - \kappa_-^{1/2}) \underline{\beta} \right\}, \quad (2.28)$$

with

$$\underline{\alpha} = \left[2\underline{\epsilon}_{\underline{\underline{cm}}} - \text{tr}(\underline{\epsilon}_{\underline{\underline{cm}}}) \underline{I} \right] \cdot \underline{A} - \text{tr}(\underline{\epsilon}_{\underline{\underline{cm}}} \cdot \underline{A}) \underline{I} - \frac{\text{tr}(\underline{\epsilon}_{\underline{\underline{cm}}}^{adj} \cdot \underline{A}) - \left[\text{tr}(\underline{\epsilon}_{\underline{\underline{cm}}}^{adj}) \text{tr}(\underline{A}) \right]}{\text{tr}(\underline{\epsilon}_{\underline{\underline{cm}}} \cdot \underline{A})} \underline{A}, \quad (2.29)$$

$$\underline{\beta} = \underline{\epsilon}_{\underline{\underline{cm}}}^{adj} - \frac{\det(\underline{\epsilon}_{\underline{\underline{cm}}})}{\text{tr}(\underline{\epsilon}_{\underline{\underline{cm}}} \cdot \underline{A})} \underline{A}, \quad (2.30)$$

$$\Delta = \left\{ \left[\text{tr}(\underline{\epsilon}_{\underline{\underline{cm}}}^{adj} \cdot \underline{A}) - \text{tr}(\underline{\epsilon}_{\underline{\underline{cm}}}^{adj}) \text{tr}(\underline{A}) \right]^2 - 4 \det(\underline{\epsilon}_{\underline{\underline{cm}}}) \text{tr}(\underline{A}) \text{tr}(\underline{\epsilon}_{\underline{\underline{cm}}} \cdot \underline{A}) \right\}^{1/2}, \quad (2.31)$$

$$\kappa_{\pm} = \mu_0 \omega^2 \frac{\left[\text{tr}(\underline{\epsilon}_{\underline{\underline{cm}}}^{adj}) \text{tr}(\underline{A}) \right] - \text{tr}(\underline{\epsilon}_{\underline{\underline{cm}}}^{adj} \cdot \underline{A}) \pm \Delta}{2 \text{tr}(\underline{A}) \text{tr}(\underline{\epsilon}_{\underline{\underline{cm}}} \cdot \underline{A})}. \quad (2.32)$$

The double integrals 2.26 and 2.28 may be evaluated using standard numerical techniques [15].

2.4 Distributional statistics

Consider the homogenization of two different material phases labelled as phase a and phase b . Both phases are considered to consist of randomly distributed, but identical orientation ellipsoidal particles. The size of the particles is specified by η , whereas the ellipsoidal shape is given by $\underline{\underline{U}}$. The space occupied by the component material a and component material b is partitioned into the disjoint regions V_a and V_b . Hence, the distributional statistics of the component phases are expressed by the characteristic functions [7]

$$\Phi_\ell(\mathbf{r}) = \begin{cases} 1, & \mathbf{r} \in V_\ell, \\ 0, & \mathbf{r} \notin V_\ell, \end{cases} \quad (\ell = a, b). \quad (2.33)$$

The n th moment of Φ_ℓ is given by the ensemble-average $\langle \Phi_\ell(\mathbf{r}_1), \dots, \Phi_\ell(\mathbf{r}_n) \rangle$ which describes the probability of $\mathbf{r}_1, \dots, \mathbf{r}_n$ inside V_ℓ . The key concept of ensemble-average is to take an average over a large number of different samples of the two component materials. The volume fraction of phase ℓ is given by the first moment of Φ_ℓ ; i.e. $\langle \Phi_\ell(\mathbf{r}) \rangle = f_\ell$ and obviously $f_a + f_b = 1$. It is noteworthy that the first moment, which only considers the volume fraction of the two components, does not give more information about the composite materials. A more comprehensive description is given by the second moment of Φ_ℓ , which provides a two-point covariance function [8]

$$\langle \Phi_\ell(\mathbf{r}) \Phi_\ell(\mathbf{r}') \rangle = \begin{cases} \langle \Phi_\ell(\mathbf{r}) \rangle \langle \Phi_\ell(\mathbf{r}') \rangle, & |\underline{\underline{U}}^{-1} \cdot (\mathbf{r} - \mathbf{r}')| > L, \\ \langle \Phi_\ell(\mathbf{r}) \rangle, & |\underline{\underline{U}}^{-1} \cdot (\mathbf{r} - \mathbf{r}')| \leq L. \end{cases} \quad (2.34)$$

The correlation length L is required to be larger than the size of the component particles but much smaller than the wavelength in order to consider the mixture is homogeneous. Certainly, higher-order moment of the Φ_ℓ give a more comprehensive statistical description of composite materials. But, in this thesis we only considered for the first and second order moments of Φ_ℓ , as higher-order moments as described elsewhere [8, 16].

2.5 Homogenization formalisms

2.5.1 Preliminaries

A composite material is formed as a mixture of component materials and yet may be considered effectively homogenous provided that wavelengths are sufficiently larger than the particle sizes of the component materials. The estimation of the constitutive parameters of such a homogenized composite material (HCM) is often derived using the very popular approaches called the Maxwell Garnett homogenization formalism and the Bruggeman homogenization formalism [1, 17]. Like most conventional approaches to homogenization, the Bruggeman formalism does not take the statistical distribution and size of the component phase particles into account. Instead, the spatial distributions are characterized by volume fraction alone and the electromagnetic response of each component particle is treated as a vanishingly small depolarization volume. Therefore, extended homogenization formalisms have been formulated in which a nonzero volume is attributed to the component phase particles [18, 19]. The electromagnetic response of an inclusion embedded in the comparison medium is usually described by the depolarization dyadic. Meanwhile, the statistical distribution of the components phases is characterized by SPFT [20].

2.5.2 Maxwell Garnett formalism

The Maxwell Garnett formalism is intended to estimate the constitutive dyadic of HCM of two component materials. Suppose material a represents an ellipsoidal inclusion characterized by shape dyadic $\underline{\underline{U}}$. The inclusions may be regarded as randomly distributed, but with identical orientation, as shown in Fig. 2.1. Meanwhile, material b is regarded as the comparison material with unspecified morphology. Thus, we introduce [4]

$$\underline{\underline{\epsilon}}_{hcm}^{MG} = \underline{\underline{\epsilon}}_b + f_a \underline{\underline{a}}_{a/b} \cdot \left(\underline{\underline{I}} - i\omega f_a \underline{\underline{D}}_{I/b}(\eta) \cdot \underline{\underline{a}}_{a,b} \right)^{-1}, \quad (2.35)$$

as the Maxwell Garnett estimate of the HCM relative permittivity of an anisotropic dielectric composite material with

$$\underline{\underline{a}}_{a/b} = (\underline{\underline{\epsilon}}_a - \underline{\underline{\epsilon}}_b) \cdot \left[\underline{\underline{I}} + i\omega \underline{\underline{D}}_{U/b}(\eta) \cdot (\underline{\underline{\epsilon}}_a - \underline{\underline{\epsilon}}_b) \right]^{-1}, \quad (2.36)$$

the polarisability dyadic and $\underline{\underline{D}}_{U/b}(\eta) \left(\underline{\underline{D}}_{I/b}(\eta) \right)$ the depolarization dyadic in the component material b .

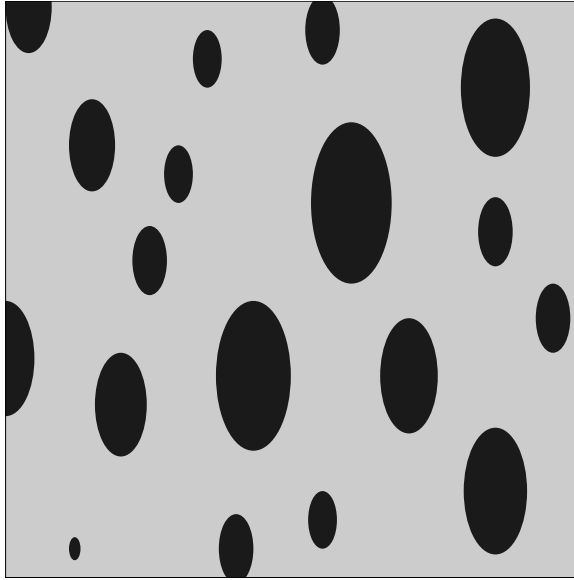


Figure 2.1: Schematic image of the component particles for the Maxwell Garnett formalism. All the ellipsoidal particles have the same shape and orientation, but randomly distributed. (Image is reprinted from [16]).



Figure 2.2: Schematic image of the component particles for the Bruggeman formalism. All material a and material b particles have the same ellipsoidal shape, but the shape for each component materials are generally different. The particles for each component materials are randomly distributed but have identical orientation. (Image is reprinted from [16]).

2.5.3 Bruggeman formalism

In the Bruggeman formalism material a and material b are treated symmetrically. That is, both materials may be regarded as randomly distributed, but with particles identical orientation as illustrated in Fig. 2.2. Furthermore, the shape dyadic of material a and material

b as specified by $\underline{\underline{U}}^a$ and $\underline{\underline{U}}^b$, respectively. Generally, $\underline{\underline{U}}^a \neq \underline{\underline{U}}^b$. Therefore, the Bruggeman estimate is generalized as [4]

$$f_a \underline{\underline{a}}_{a,Br} + f_b \underline{\underline{a}}_{b,Br} = 0, \quad (2.37)$$

with polarisabilities

$$\underline{\underline{a}}_{a,Br} = \left(\underline{\underline{\epsilon}}_a - \underline{\underline{\epsilon}}_{hcm}^{Br} \right) \cdot \left[\underline{\underline{I}} + i\omega \underline{\underline{D}}_{\underline{\underline{U}}^a/Br}(\eta) \cdot \left(\underline{\underline{\epsilon}}_a - \underline{\underline{\epsilon}}_{hcm}^{Br} \right) \right]^{-1}, \quad (2.38)$$

$$\underline{\underline{a}}_{b,Br} = \left(\underline{\underline{\epsilon}}_b - \underline{\underline{\epsilon}}_{hcm}^{Br} \right) \cdot \left[\underline{\underline{I}} + i\omega \underline{\underline{D}}_{\underline{\underline{U}}^b/Br}(\eta) \cdot \left(\underline{\underline{\epsilon}}_b - \underline{\underline{\epsilon}}_{hcm}^{Br} \right) \right]^{-1}. \quad (2.39)$$

In solving the nonlinear dyadic Eq. 2.37 for $\underline{\underline{\epsilon}}_{hcm}^{Br}$, the common solution method is Jacobi iteration [21]. Thus, the iterative solution is

$$\underline{\underline{\epsilon}}_{hcm}^{Br}(n) = F \left\{ \underline{\underline{\epsilon}}_{hcm}^{Br}(n-1) \right\}, \quad (n = 1, 2, \dots), \quad (2.40)$$

where

$$F \left\{ \underline{\underline{\epsilon}}_{hcm}^{Br} \right\} = \left\{ f_a \underline{\underline{\epsilon}}_a \cdot \left[\underline{\underline{I}} + i\omega \underline{\underline{D}}_{\underline{\underline{U}}^a/Br}(\eta) \cdot \left(\underline{\underline{\epsilon}}_a - \underline{\underline{\epsilon}}_{hcm}^{Br} \right) \right]^{-1} + f_b \underline{\underline{\epsilon}}_b \cdot \left[\underline{\underline{I}} + i\omega \underline{\underline{D}}_{\underline{\underline{U}}^b/Br}(\eta) \cdot \left(\underline{\underline{\epsilon}}_b - \underline{\underline{\epsilon}}_{hcm}^{Br} \right) \right]^{-1} \right\} \\ \left\{ f_a \left[\underline{\underline{I}} + i\omega \underline{\underline{D}}_{\underline{\underline{U}}^a/Br}(\eta) \cdot \left(\underline{\underline{\epsilon}}_a - \underline{\underline{\epsilon}}_{hcm}^{Br} \right) \right]^{-1} + f_b \left[\underline{\underline{I}} + i\omega \underline{\underline{D}}_{\underline{\underline{U}}^b/Br}(\eta) \cdot \left(\underline{\underline{\epsilon}}_b - \underline{\underline{\epsilon}}_{hcm}^{Br} \right) \right]^{-1} \right\}^{-1}, \quad (2.41)$$

and $\underline{\underline{\epsilon}}_{hcm}^{Br}(0) = \underline{\underline{\epsilon}}_{hcm}^{MG}$.

2.5.4 Strong Property Fluctuation theory

A more sophisticated approach to homogenization is provided by SPFT. As for the Bruggeman formalism, SPFT treats the two component material symmetrically, but in higher-order implementations of the SPFT, the shapes and orientations of both component material a and material b particles need to be the same (i.e., $\underline{\underline{U}}^a = \underline{\underline{U}}^b$). Therefore, the Bruggeman formalism can also be thought of SPFT, but at the lowest order of approximation. A schematic illustration of SPFT is given in Fig. 2.3.

SPFT accommodates the distributional statistics of the particles of the component phases contained by material a and material b . That means, the HCM constitutive parameters are estimated by iterative refinements of the comparison material. The iterations are expressed in term of correlation functions. The two-point covariance function 2.34 along with the correlation length L , describes the statistical geometry of material a and material b and is often implemented to the second order of SPFT. Thus, the second order SPFT estimates of

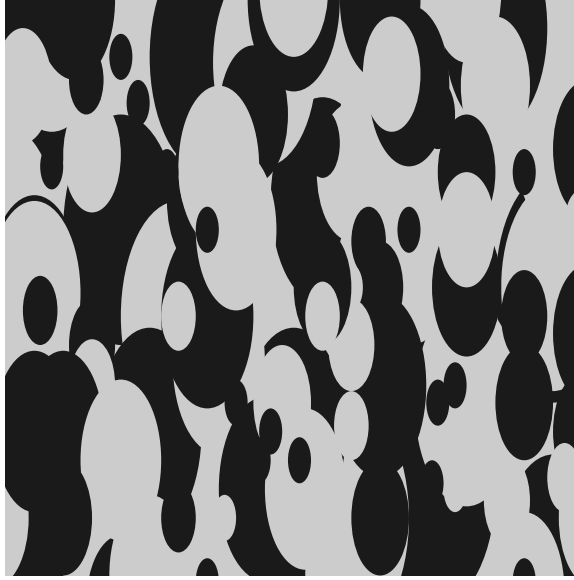


Figure 2.3: Schematic image of the component particles for the SPFT. All material a and material b particles have the same ellipsoidal shape. The particles for each component material are randomly distributed, but have identical orientation. (Image is reprinted from [16]).

the constitutive dyadic of the HCM is given by [22]

$$\underline{\underline{\epsilon}}_{hcm}^{SPFT[2]} = \underline{\underline{\epsilon}}_{cm} - \frac{1}{i\omega} \left(\underline{\underline{I}} + \underline{\underline{\Sigma}}^{[2]} \cdot \underline{\underline{D}}_{U/cm}^\eta(\eta) \right)^{-1} \cdot \underline{\underline{\Sigma}}^{[2]}. \quad (2.42)$$

Herein, $\underline{\underline{\Sigma}}^{[2]}$ is the second order mass operator provided by [23]

$$\underline{\underline{\Sigma}}^{[2]} = f_a f_b \left(\underline{\underline{a}}_{a/cm} - \underline{\underline{a}}_{b/cm} \right) \cdot \underline{\underline{D}}_{U/cm}^\eta \cdot \left(\underline{\underline{a}}_{a/cm} - \underline{\underline{a}}_{b/cm} \right), \quad (2.43)$$

with polarisability density dyadics

$$\underline{\underline{a}}_{a/cm} = i\omega \left(\underline{\underline{\epsilon}}_a - \underline{\underline{\epsilon}}_{cm} \right) \cdot \left[\underline{\underline{I}} + i\omega \underline{\underline{D}}_{U/cm}^\eta(\eta) \cdot \left(\underline{\underline{\epsilon}}_a - \underline{\underline{\epsilon}}_{cm} \right) \right]^{-1}, \quad (2.44)$$

$$\underline{\underline{a}}_{b/cm} = i\omega \left(\underline{\underline{\epsilon}}_b - \underline{\underline{\epsilon}}_{cm} \right) \cdot \left[\underline{\underline{I}} + i\omega \underline{\underline{D}}_{U/cm}^\eta(\eta) \cdot \left(\underline{\underline{\epsilon}}_b - \underline{\underline{\epsilon}}_{cm} \right) \right]^{-1}. \quad (2.45)$$

The mass operator $\underline{\underline{\Sigma}}^{[n]}$ is null at the zeroth and first order [9]. Hence, $\underline{\underline{\epsilon}}_{hcm}^{SPFT[0]} = \underline{\underline{\epsilon}}_{hcm}^{SPFT[1]} = \underline{\underline{\epsilon}}_{cm}$ for which the constitutive parameters of the comparison material $\underline{\underline{\epsilon}}_{cm}$ are provided by Bruggeman formalism estimation $\underline{\underline{\epsilon}}_{hcm}^{Br}$ [9]. The depolarization dyadic $\underline{\underline{D}}_{U/cm}^\eta(\eta)$ in 2.42 and 2.43 corresponds to component particles with the same shape dyadic $\underline{\underline{U}}$ in the comparison material.

2.6 Conclusion

In this chapter we described the homogenization formalisms used in the later chapters of this thesis. These mathematical constructions will be implemented for certain dielectric materials with a view to optical sensing applications.



Chapter 3

The Bruggeman formalism for inverse homogenization

A composite material is formed as a mixture of component materials. Its may be regarded as being effectively homogeneous when wavelengths are sufficiently larger than the particle sizes of the component materials that make up the composite material. The estimation of the constitutive parameters of such a homogenized composite material (HCM) is often derived using a very widely applied homogenization formalism approach called the Bruggeman formalism [2, 24], from a knowledge of the constitutive parameters of its component materials, along with a knowledge of the distributional statistics and shapes of its component particles [2, 22]. Applications of Bruggeman formalism are continuing to emerge, for examples, in recent developments pertaining to complex HCMs [25, 26] and negatively-refracting metamaterials [22, 27]. However, a certain limitation of the Bruggeman homogenization formalism was reported in 2004 for isotropic dielectric HCMs [28]. The manifestation of physically-implausible Bruggeman estimates resulted from the choice of constitutive parameters for the component materials and independent of the distributional statistics or shapes of the component particles. This limitation which is also relevant to active [29] and anisotropic [30] HCMs, also extends to the Maxwell Garnett homogenization formalism which shares a common provenance with the Bruggeman formalism [17].

In this chapter, we investigate the applicability of the Bruggeman formalism to the inverse homogenization scenario wherein the relative permittivity of one of the component materials is estimated from a knowledge the relative permittivities of the other component material and the HCM. We restrict our attention to the simplest possible case of an isotropic dielectric HCM arising from two isotropic dielectric component materials. Formal expressions have

been established for the inverse Bruggeman formalism (and the inverse Maxwell Garnett formalism) in the general setting of bianisotropic HCMs [31], but in certain cases these formal expressions may be ill-posed [32] and the ranges of applicability of these inverse formalisms have not been established. Generally, inverse problems may be ill-posed even when the corresponding forward problems are well-posed [33]. However, the inverse Bruggeman formalism is fundamentally different to the forward Bruggeman formalism as further described in Sec. 3.1 and some illustrative numerical examples in Sec. 3.2. Our study is partly motivated by very recent implementations of the inverse Bruggeman formalism in estimating nanoscale constitutive and morphological parameters of certain sculptured thin films [34], which is a key step in modelling the electromagnetic response of infiltrated sculptured thin films [35, 36].

3.1 Theory

We consider the homogenization of two isotropic dielectric component materials with relative permittivities ϵ_a and ϵ_b . The component materials a and b are assumed to be distributed randomly as spherical particles with volume fractions f_a and $f_b = 1 - f_a$, respectively. The Bruggeman estimate of the relative permittivity of the corresponding HCM, namely ϵ_{hcm}^{Br} , is provided via [24]

$$f_a \frac{\epsilon_a - \epsilon_{hcm}^{Br}}{\epsilon_a + 2\epsilon_{hcm}^{Br}} + f_b \frac{\epsilon_b - \epsilon_{hcm}^{Br}}{\epsilon_b + 2\epsilon_{hcm}^{Br}} = 0, \quad (3.1)$$

which is nonlinear in ϵ_{hcm}^{Br} . A straightforward manipulation of 3.1 delivers the explicit formula

$$\epsilon_a = \frac{(f_a - 2f_b)\epsilon_b + 2\epsilon_{hcm}^{Br}}{f_b(\epsilon_b - \epsilon_{hcm}^{Br}) + f_a(\epsilon_b + 2\epsilon_{hcm}^{Br})} \epsilon_{hcm}^{Br} \quad (3.2)$$

for ϵ_a in terms of ϵ_b , ϵ_{hcm}^{Br} , f_a and f_b . Since the component materials a and b are treated in an identical manner within the Bruggeman formalism, the corresponding formula for ϵ_b has the same form as 3.2. Notice that as the inverse Bruggeman equation 3.2 does not involve a square root, there is no scope for $\text{Im}\{\epsilon_a\}$ being nonzero if $\epsilon_b, \epsilon_{hcm}^{Br} \in \mathbb{R}$. This contrasts with the forward Bruggeman formalism where a square root term enables $\text{Im}\{\epsilon_{hcm}^{Br}\}$ to be nonzero even though $\epsilon_a, \epsilon_b \in \mathbb{R}$. This physically-implausible scenario can arise when $\epsilon_a/\epsilon_b < 0$ [28]. Consequently, the explicit formula 3.2 provides the inverse formalism estimate of ϵ_a or ϵ_b whereas the forward formalism estimate of the relative permittivity of the HCM is provided by selecting a root of a quadratic equation. Therefore, the range of applicability of the inverse

Bruggeman formalism cannot be inferred from a knowledge of the range of applicability of the forward Bruggeman formalism.

For comparison, we introduce the Maxwell Garnett estimate of the HCM relative permittivity [24]

$$\epsilon_{hcm}^{MG} = \epsilon_b + \frac{3f_a\epsilon_b(\epsilon_a - \epsilon_b)}{\epsilon_a + 2\epsilon_b - f_a(\epsilon_a - \epsilon_b)} \quad (3.3)$$

and its corresponding inverse

$$\epsilon_a = \frac{(2 + f_a)\epsilon_{hcm}^{MG} - 2f_b\epsilon_b}{(1 + 2f_a)\epsilon_b - f_b\epsilon_{hcm}^{MG}} \epsilon_b. \quad (3.4)$$

The limiting behaviour of the inverse Bruggeman estimate 3.2 as compared with that of the inverse Maxwell Garnett estimate 3.4 is especially revealing. In the limit $f_a \rightarrow 1$, both estimates yield the relative permittivity of the HCM, as they must¹. In the limit $f_a \rightarrow 0$, the inverse Bruggeman formalism yields $\epsilon_a \rightarrow -2\epsilon_{hcm}^{Br}$ whereas the inverse Maxwell Garnett formalism yields $\epsilon_a \rightarrow -2\epsilon_b$. Therefore, the two inverse estimates differ markedly as f_a approaches zero, provided that ϵ_b and the relative permittivity of the HCM are sufficiently different.

3.2 Numerical studies

For our numerical studies, we explore the inverse Bruggeman estimate 3.2, in comparison with the inverse Maxwell Garnett estimate 3.4, by means of some illustrative numerical examples. We consider three different scenarios. First is nondissipative homogenization scenarios, followed by dissipative homogenization scenarios and finally the scenario when $\text{Re}\{\epsilon_{hcm}^{Br, MG}\} / \text{Re}\{\epsilon_b\} < 0$. For nondissipative scenarios, the forward Bruggeman formalism runs into difficulties when $\epsilon_a/\epsilon_b < 0$, but not when $\epsilon_a/\epsilon_b > 0$ [28]. Accordingly, let us begin by focussing on the regimes $\epsilon_{hcm}^{Br, MG}/\epsilon_b < 0$ and $\epsilon_{hcm}^{Br, MG}/\epsilon_b > 0$. In Fig. 3.1, plots of ϵ_a , as determined by the inverse Bruggeman formalism and the inverse Maxwell Garnett formalism, versus f_a are provided for the cases where $\epsilon_b = \pm 2$ and $\epsilon_{hcm}^{Br, MG} = 3$. When $\epsilon_{hcm}^{Br, MG}/\epsilon_b > 0$ the inverse Bruggeman and inverse Maxwell Garnett estimates are in fairly close agreement. However, the values of ϵ_a yielded by the two inverse formalisms differ markedly when $\epsilon_{hcm}^{Br, MG}/\epsilon_b < 0$, except in the limit as f_a approaches unity. Most notably, the inverse Brugge-

¹The Maxwell Garnett estimate of the HCM relative permittivity is only strictly applicable in the dilute composite regime $f_a \lesssim 0.3$. Accordingly, estimates of ϵ_a delivered by the inverse Maxwell Garnett formalism are strictly valid only for $f_a \lesssim 0.3$. However, ϵ_{hcm}^{MG} coincides with one of the Hashin-Shtrikman bounds on the HCM relative permittivity which applies at all values of f_a [37].

man estimate becomes singular and undergoes a change in sign as the volume fraction increases through $f_a = 0.56$, whereas the inverse Maxwell Garnett value remains finite and does not change sign.

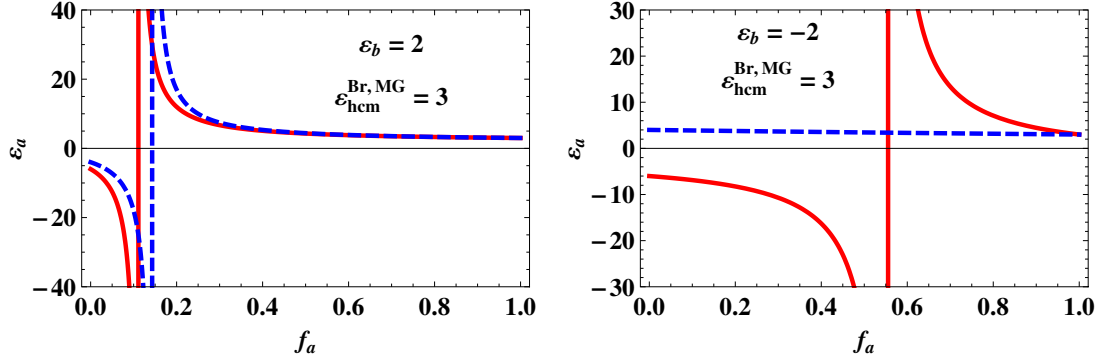


Figure 3.1: Plots of ϵ_a as determined by the inverse Bruggeman formalism (red, solid curves) and the inverse Maxwell Garnett formalism (blue, dashed curves) versus f_a for $\epsilon_b = \pm 2$ and $\epsilon_{hcm}^{Br, MG} = 3$. Estimates of ϵ_a delivered by the inverse Maxwell Garnett formalism are strictly valid only for $f_a \lesssim 0.3$.

Next we turn to dissipative homogenization scenarios. In the case of the forward Bruggeman formalism, problems arise when $\text{Re}\{\epsilon_a\}/\text{Re}\{\epsilon_b\} < 0$ and the degree of dissipation is relatively small. If $\text{Re}\{\epsilon_a\}/\text{Re}\{\epsilon_b\} < 0$ and the degree of dissipation is relatively large or if $\text{Re}\{\epsilon_a\}/\text{Re}\{\epsilon_b\} > 0$, then the forward Bruggeman formalism was found to deliver physically-plausible estimates of the HCM relative permittivity [28]. Accordingly, we consider the regimes where $\text{Re}\{\epsilon_{hcm}^{Br, MG}\}/\text{Re}\{\epsilon_b\} > 0$ with the degree of dissipation in the HCM being relatively small, moderate and large. Graphs of the real and imaginary parts of ϵ_a , as estimated by the inverse Bruggeman and inverse Maxwell Garnett formalisms, are plotted versus f_a in Fig. 3.2 for the cases $\epsilon_b = 2$ and $\epsilon_{hcm}^{Br, MG} = 3 + \delta i$ where $\delta \in \{0.1, 1, 10\}$. When the degree of HCM dissipation is relatively small ($\delta = 0.1$), the estimates of the real and imaginary parts of ϵ_a provided by the inverse Bruggeman and inverse Maxwell Garnett formalisms agree fairly closely. When the degree of HCM dissipation is moderate ($\delta = 1$), there is still fairly close agreement between the inverse Bruggeman and inverse Maxwell Garnett values of ϵ_a for most values of f_a . Crucially, however, for $f_a < 0.05$ the imaginary part of ϵ_a estimated by the inverse Bruggeman formalism is negative-valued (unlike $\text{Im}\{\epsilon_a\}$ estimated by the inverse Maxwell Garnett formalism which is positive-valued). Here $\text{Im}\{\epsilon_a\} < 0$ is not a physically-plausible outcome as it implies that the homogenization of an active material a and a nondissipative material b results in a dissipative HCM. For both the real and imaginary parts of ϵ_a , the discrepancies between the values estimated by the two inverse formalisms become enormous when the degree of HCM dissipation is relatively large ($\delta = 10$). Furthermore, the inverse Bruggeman

estimate is physically implausible for a much larger range of f_a values; i.e., $\text{Im}\{\epsilon_a\}$ estimated by inverse Bruggeman formalism is negative-valued for $f_a < 0.3$ when $\delta = 10$.

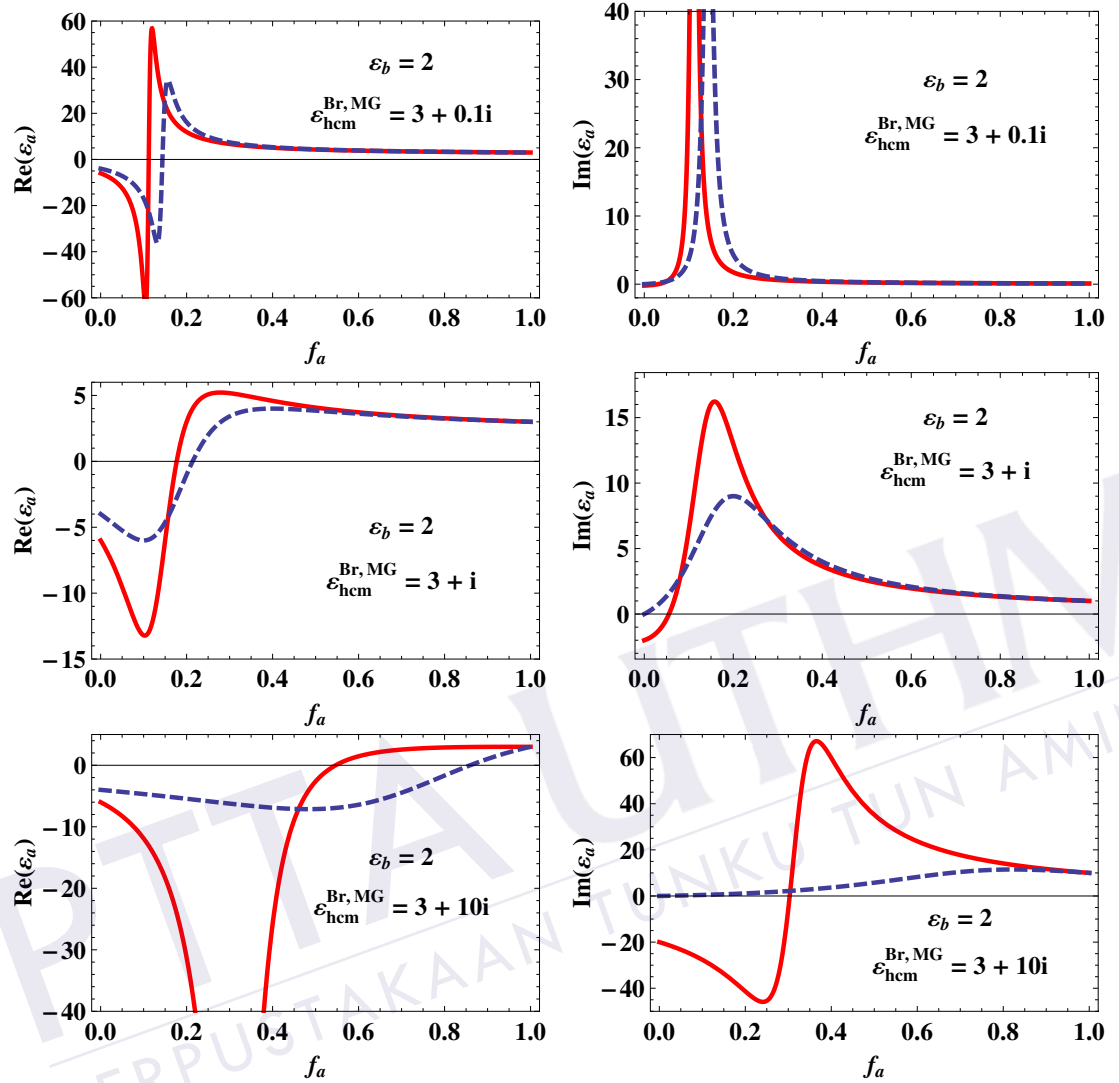


Figure 3.2: Plots of the real and imaginary parts of ϵ_a as determined by the inverse Bruggeman formalism (red, solid curves) and the inverse Maxwell Garnett formalism (blue, dashed curves) versus f_a for $\epsilon_b = 2$ and $\epsilon_{hcm}^{Br, MG} = 3 + \delta i$ where $\delta \in \{0.1, 1, 10\}$. Estimates of ϵ_a delivered by the inverse Maxwell Garnett formalism are strictly valid only for $f_a \lesssim 0.3$.

Lastly, we explore the $\text{Re}\{\epsilon_{hcm}^{Br, MG}\} / \text{Re}\{\epsilon_b\} < 0$ regime. Plots of the real and imaginary values of ϵ_a in Fig. 3.3 correspond to the same parameter values as those used for Fig. 3.2 except that here $\epsilon_b = -2$. The estimates of the inverse Bruggeman formalism are now physically implausible due to $\text{Im}\{\epsilon_a\} < 0$ for a wide range of f_a values, regardless of whether the degree of HCM dissipation is relatively small, moderate or large. In contrast, the estimate of $\text{Im}\{\epsilon_a\}$ provided by the inverse Maxwell Garnett formalism is positive-valued for all scenarios considered. Additionally, the real parts of ϵ_a delivered by the two inverse formalisms differ

enormously except when f_a approaches unity, for all degrees of HCM dissipation considered.

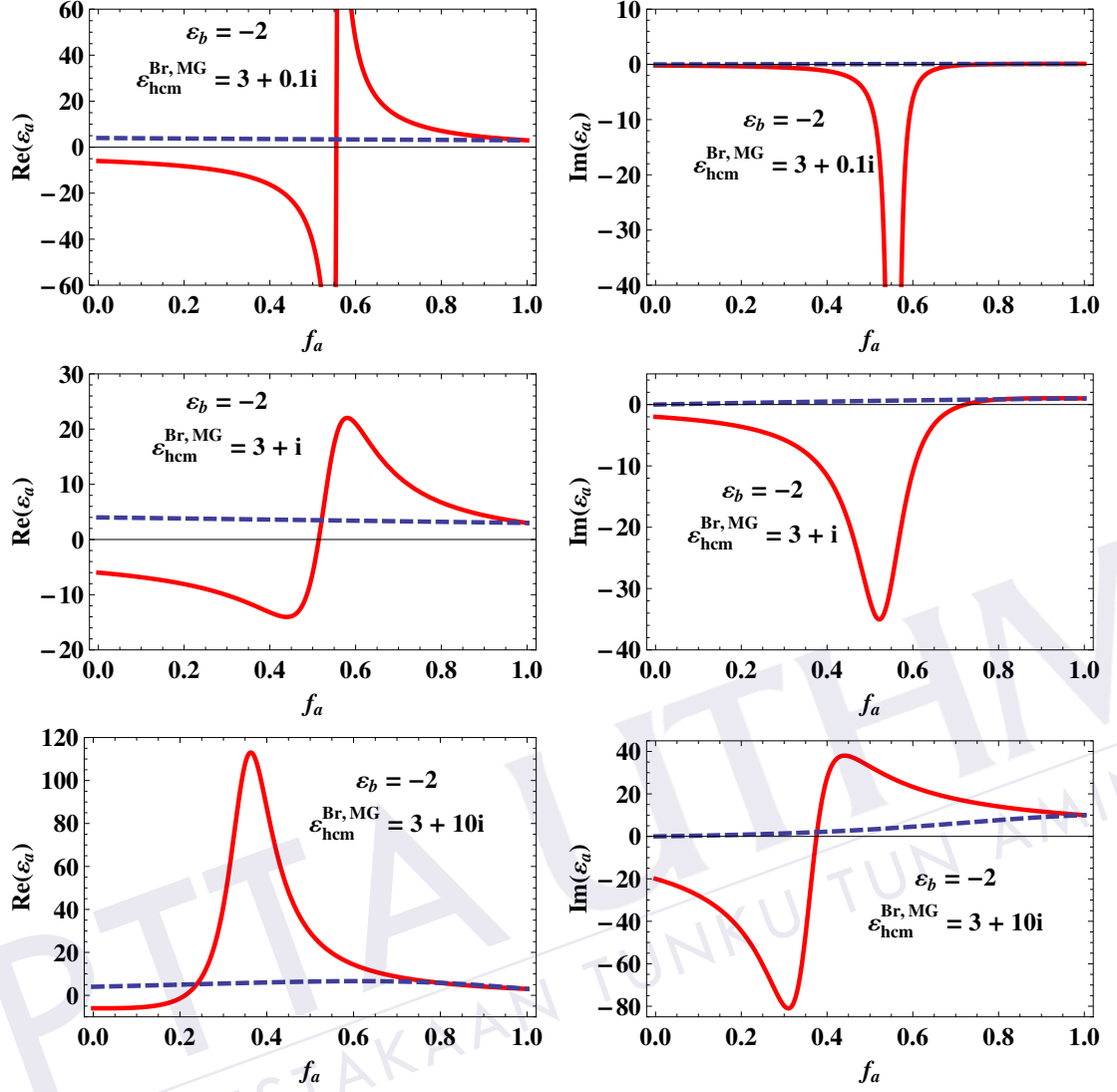


Figure 3.3: As Fig. 3.2 except that $\epsilon_b = -2$.

3.3 Closing remarks

From our numerical studies, we have found that in the case of dissipative HCMs, the inverse Bruggeman estimates of ϵ_a can be physically implausible when

- (i) $\text{Re}\{\epsilon_{hcm}^{Br}\} / \text{Re}\{\epsilon_b\} > 0$ and the degree of HCM dissipation is moderate or greater; or
- (ii) $\text{Re}\{\epsilon_{hcm}^{Br}\} / \text{Re}\{\epsilon_b\} < 0$ regardless of the degree of HCM dissipation.

In the case of nondissipative HCMs, enormous discrepancies can exist between the estimates of ϵ_a provided by the inverse Bruggeman formalism and the inverse Maxwell Garnett formalism when $\epsilon_{hcm}^{Br, MG} / \epsilon_b < 0$. The constitutive parameters chosen in Sec. 3.2 to illustrate the

limitations of the inverse Bruggeman formalism were representative examples. Further numerical studies for other choices of constitutive parameters conforming to scenarios (i) and (ii) (presented in Appendix A) yielded qualitatively similar results. Therefore, we conclude that the inverse Bruggeman formalism should be applied with great caution.

Finally, we note that in the very recent implementations of the inverse Bruggeman formalism which motivated this study [34, 35, 36], the relative permittivity parameters were positive-valued and the materials were nondissipative. The estimates yielded by the inverse Bruggeman formalism in these cases seem physically plausible, but the acid test can only be provided by suitable experimental measurements.



Chapter 4

Sculptured thin films

4.1 Introduction

Sculptured thin films (STFs) are nanostructured materials with anisotropic and unidirectionally nonhomogenous which can be designed and fabricated using physical vapour deposition (PVD) techniques. In a controllable manner, various columnar morphologies of STF can be formed in 2D and 3D [38], which have been termed as sculptured nematic thin films (SNTFs) [39] and thin-film helicoidal bianisotropic medium (TFHBMs) [40, 41], respectively. For example, slanted columns, chevrons, C-shaped, S-shaped and zigzag for 2D STFs while helixes and superhelixes are examples for 3D STFs [42]. In this chapter, we provide a rough introduction of the simple slanted columns known as columnar thin films (CTFs) as well as the more complex shape known as chiral sculptured thin films (CSTFs). These two types of STF are implemented in our studies in the following chapters of this thesis. Homogenization studies on STFs with particular to estimate their constitutive parameters are also presented in this chapter.

4.2 Columnar thin films

CTF was first studied during the 1960s [43]. It consists of a parallel array of columnar nanowires which may be grown on the substrate by directing the vapour flux at an angle χ_v to a fixed substrate during PVD. Under certain conditions, parallel columns are oriented at angle $\chi \geq \chi_v$ to a planar substrate [42] (see Fig. 4.1). Furthermore, through judicious control of the vapour deposition process, both the macroscopic optical properties and the porosity of the CTF can be tailored to order [45]. Consequently, CTFs are promising candidates as platforms for optical sensing applications, wherein it is envisaged that the species to be

sensed is contained within a fluid which penetrates the void regions in between the CTF's columns for which the column diameter can range from 10 to 300 nm.

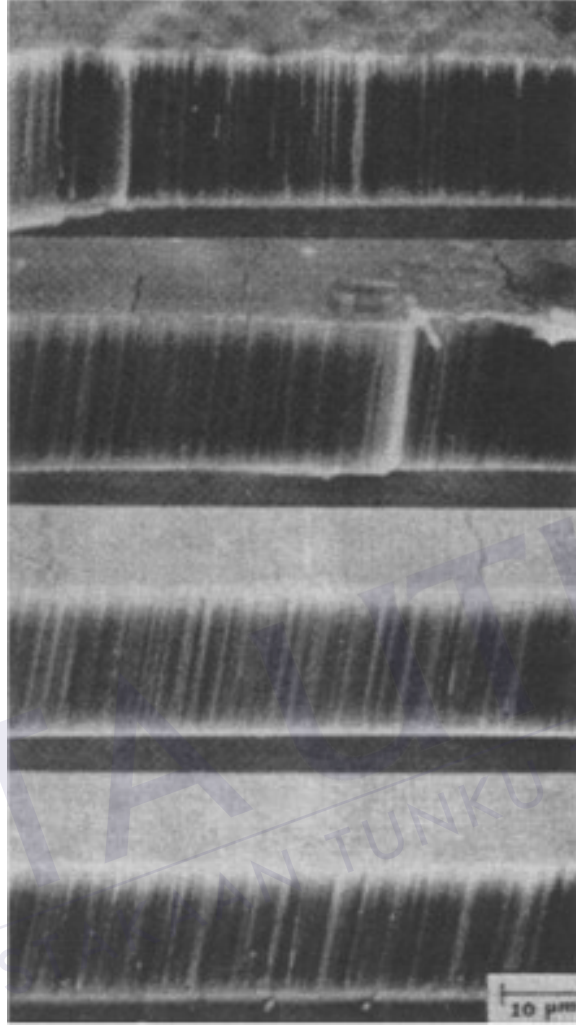



Figure 4.1: Scanning electron micrograph of CTF. (Image is reprinted from [44])

A recent theoretical investigation highlighted the fact that surface-plasmon-polariton (SPP) waves (see Appendix B for further details), guided by the planar interface of an infiltrated CTF and a thin layer of metal, may be usefully harnessed for optical sensing [36]. In this scenario, the angle of incidence required to excite an SPP wave was found to be acutely sensitive to changes in the refractive index n_ℓ of the fluid which fills the CTF's void regions. Furthermore, the phase speed and propagation length of the SPP wave were also sensitive to n_ℓ .

Bibliography

- [1] A. Sihvola, Electromagnetic mixing formulas and applications, IEE, London, UK (1999).
- [2] A. Lakhtakia, ed., Selected papers on linear optical composite materials, SPIE Press, Bellingham, WA (1996).
- [3] G. W. Milton, The theory of composites, Cambridge University Press, Cambridge, UK (2002).
- [4] W. S. Weiglhofer, A. Lakhtakia and B. Michel, Maxwell Garnett and Bruggeman formalisms for a particulate composite with bianisotropic host medium, *Micro. Opt. Technol.* 15 (1997) 1263–1266. Erratum: 22 (1999) 221.
- [5] B. Michel, A Fourier space approach to the pointwise singularity of an anisotropic dielectric medium, *Int. J. Appl. Electromag. Mech.* 8 (1997) 219–227.
- [6] B. Michel and W. S. Weiglhofer, Pointwise singularity of dyadic Green function in a general bianisotropic medium, *Int. J. Electron. Commun.* 51 (1997) 219–223. Erratum: 52 (1998) 31.
- [7] B. Michel and A. Lakhtakia, Strong-property-fluctuation theory for homogenizing chiral particulate composites, *Phys. Rev. E* 51 (1995) 5701–5707.
- [8] L. Tsang, J. A. Kong and R. W. Newton, Application of strong fluctuation random medium theory to scattering of electromagnetic waves from a half-space of dielectric mixture, *IEEE Trans. Antennas Propagate* 30 (1982) 292–302.
- [9] T. G. Mackay, A. Lakhtakia and W. S. Weiglhofer, Strong-property-fluctuation theory for homogenization of bianisotropic composites: formulation, *Phys. Rev. E* 62 (2000) 6052–6064. Erratum: 63 (2001) 049901.
- [10] D. Fleisch, A Student's guide to Maxwell's equations, Cambridge University Press, Cambridge, UK (2008).

- 
- [11] H. C. Chen, Theory of electromagnetic waves: A coordinate-free approach, McGraw-Hill, USA (1983).
- [12] T. G. Mackay and A. Lakhtakia, Electromagnetic anisotropy and bianisotropy: A field guide, World Scientific, Singapore (2010).
- [13] E. Kreyszig, Advance engineering mathematics, 9th ed., John Wiley & Sons, Inc., Singapore (2006).
- [14] T. G. Mackay, Depolarization volume and correlation length in the homogenization of an anisotropic dielectric composites, Waves Random Media 14 (2004) 485–498. Erratum: 16 (2006) 85.
- [15] W. H. Press, B. P. Flannery, S. A. Teukolsky and W. T. Vetterling, Numerical recipes in Fortran, 2nd. ed., Cambridge University Press, Cambridge, UK (1992).
- [16] T. G. Mackay, Effective constitutive parameters of linear nanocomposite in the long-wavelength regime, J. Nanophoton. 5 (2011) 051001-1–051001-25.
- [17] D. E. Aspén, Local-field effects and effective-medium theory: A microscopic perspective, Am. J. Phys. Vol. 50 (1982) 704–709.
- [18] B. Shanker and A. Lakhtakia, Extended Maxwell Garnett model for chiral-in-chiral composites, J. Phys. D: Appl. Phys. 26 (1993) 1746–1758.
- [19] B. Shanker, The extended Bruggeman approach for chiral-in-chiral mixtures, J. Phys. D: Appl. Phys. 29 (1996) 281–288.
- [20] L. Tsang and J. A. Kong, Scattering of electromagnetic waves from random media with strong permittivity fluctuations, Radio Sci. 16 (1981) 303–320.
- [21] B. Michel, A. Lakhtakia and W. S. Weiglhofer, Homogenization of linear bianisotropic particulate composite media — Numerical studies, Int. J. Appl. Electromag. Mech. 9 (1998) 167–178. Erratum: 10 (1999) 537–538.
- [22] T. G. Mackay, Linear and nonlinear homogenized composite mediums as metamaterials, Electromagnetics 25 (2005) 461–481.
- [23] U. Frisch, Wave propagation in random media, Probabilistic methods in applied mathematics, A. T. Bharucha-Reid (ed.), (London, UK: Academic Press), 1 (1970) 75–198.

- [24] L. Ward, The optical constants of bulk materials and films, 2nd ed., Institute of Physics, Bristol, UK (2000).
- [25] W. S. Weiglhofer and T. G. Mackay, Numerical studies of the constitutive parameters of a chiroplasma composite medium, *ÆŮ — Int. J. Electron. Commun.* 54 (2000) 259–265.
- [26] T. G. Mackay and W. S. Weiglhofer, Homogenization of biaxial composite materials: dissipative anisotropic properties, *J. Opt. A: Pure Appl. Opt.* 2 (2000) 426–432.
- [27] T. G. Mackay and A. Lakhtakia, Negative phase velocity in isotropic dielectric-magnetic media via homogenization, *Microwave Opt. Technol. Lett.* 47 (2005) 313–315.
- [28] T. G. Mackay and A. Lakhtakia, A limitation of the Bruggeman formalism for homogenization, *Opt. Commun.* 234 (2004) 35–42. Erratum: 282 (2009) 4028.
- [29] T. G. Mackay and A. Lakhtakia, On the application of homogenization formalisms to active dielectric composite materials, *Opt. Commun.* 282 (2009), 2470–2475.
- [30] T. G. Mackay, A. Lakhtakia and A. J. Duncan, On limitations of conventional approaches to homogenization applied to uniaxial dielectric composite materials, *Proc. SPIE* 7404 (2009) 740406.
- [31] W. S. Weiglhofer, On the inverse homogenization problem of linear composite materials, *Microwave Opt. Technol. Lett.* 28 (2001) 421–423.
- [32] E. Cherkaev, Inverse homogenization for evaluation of effective properties of a mixture, *Inverse Problems* 17 (2001) 1203–1218.
- [33] A. Tarantola, Inverse problem theory and methods for model parameter estimation, SIAM, Philadelphia, PA (2005).
- [34] T. G. Mackay and A. Lakhtakia, Determination of constitutive and morphological parameters of columnar thin films by inverse homogenization, *J. Nanophoton.* 4 (2010) 041535.
- [35] T. G. Mackay and A. Lakhtakia, Empirical model of optical sensing via spectral shift of circular Bragg phenomenon, *IEEE Photonics J.* 2 (2010) 92–101.
- [36] T. G. Mackay and A. Lakhtakia, Modeling columnar thin films as platforms for surface-plasmonic-polaritonic optical sensing, *Photon. Nanostruct. Fundam. Appl.* 8 (2010) 140–149.

- [37] Z. Hashin and S. Shtrikman, A variational approach to the theory of the effective magnetic permeability of multiphase materials, *J. Appl. Phys.* 33 (1962) 3125–313.
- [38] A. Lakhtakia and R. Messier, Sculptured thin films — I. Concepts, *Mat. Res. Innovat.* 1 (1997) 145–148.
- [39] R. Messier, T. Gehrke, C. Frankel, V. C. Venugopal, W. Otano and A. Lakhtakia, Engineered sculptured nematic thin films, *J. Vac. Sci. Technol. A* 15 (1997) 2148–2152.
- [40] A. Lakhtakia and R. Messier, The key to a thin film HBM: the Motohiro-Taga interface, *Proceedings of Chiral '94: 3rd International workshop on chiral, bi-isotropic and bi-anisotropic media* (F. Mariotte and J.-P. Parneix, eds), Perigueux, France, (1994) 125–130.
- [41] K. Robbie, M. J. Brett and A. Lakhtakia, First thin film realisation of a helicoidal bian-isotropic medium, *J. Vac. sci. Technol. A* 13 (1995) 2991–2993.
- [42] A. Lakhtakia and R. Messier, *Sculptured thin films: Nanoengineered morphology and optics*, SPIE Press, Bellingham, WA, USA (2005).
- [43] R. H. Wade and J. Silcox, Columnar structure in thin vacuum–condensed Pd films, *Appl. Phys. Lett.* 8 (1966) 7–10.
- [44] J.A. Polo Jr. and A. Lakhtakia, Morphological effects on surface-plasmon-polariton waves at the planar interface of a metal and a columnar thin film, *Opt. Commun.* 281 (2008) 5453–5457.
- [45] G. B. Smith, Theory of angular selective transmittance in oblique columnar thin films containing metal and voids, *Appl. Opt.* 29 (1990) 3685–3693.
- [46] P. J. Collings, *Liquid crystals: Nature's delicate phase of matter*, 2nd edition, Princeton Univ. Press, New Jersey, USA (2002).
- [47] N. O. Young and J. Kowal, Optically active fluorite films, *Nature* 183 (1959) 104–105.
- [48] K. Robbie, M. J. Brett and A. Lakhtakia, Chiral sculptured thin film, *Nature* 384 (1996) 616.
- [49] A. Lakhtakia, Sculptured thin films: accomplishments and emerging uses, *Mat. Sci. and Eng. C* 1 (2002) 417–434.
- [50] A. Lakhtakia and R. Messier, Sculptured thin films — II. Experiments and applications, *Mat. Res. Innovat.* 2 (1999) 217–222.

- [51] A. Lakhtakia, On bioluminescent emission from chiral sculptured thin films, *Opt. Commun.* 188 (2001) 313–320.
- [52] T. G. Mackay and A. Lakhtakia, Theory of light emission from a dipole source embedded in a chiral sculptured thin film, *Opt. Express*, 15 (2007) 14689–14703. Erratum: 16 (2008) 3659.
- [53] T. G. Mackay and A. Lakhtakia, Modeling chiral sculptured thin films as platforms for surface-plasmonic-polaritonic optical sensing, *IEEE Sensors J.* 12 (2012) 273–280.
- [54] A. Lakhtakia and J. A. Polo Jr., Morphological influence on surface-wave propagation at the planar interface of a metal film and a columnar thin film, *Asian J. Phys.* 17 (2008) 185–191. (The value of $\text{Im}[\kappa]$ for $\chi_\nu = 5^\circ$ presented in Table 1 should be 0.0108.)
- [55] P. G. de Gennes and J. Prost, *The physics of liquid crystals*, 2nd ed., Oxford Univ. Press, New York, NY, USA (1993).
- [56] J. A. Sherwin, A. Lakhtakia and I. J. Hodgkinson, On calibration of a nominal structure-property relationship model for chiral sculptured thin films by axial transmittance measurements, *Opt. Commun.* 209 (2002) 369–375.
- [57] I. Hodgkinson, Q. h. Wu and J. Hazel, Empirical equations for the principal refractive indices and column angle of obliquely deposited films of tantalum oxide, titanium oxide, and zirconium oxide, *Appl. Opt.* 37 (1998) 2653–2659.
- [58] A. Lakhtakia, Enhancement of optical activity of chiral sculptured thin films by suitable infiltration of void regions, *Optik* 112 (2001) 145–148. Erratum: 112 (2001) 544.
- [59] T. G. Mackay and A. Lakhtakia, Electromagnetic fields in linear bianisotropic mediums, *Prog. Opt.* 51 (2008) 121–209.
- [60] T. G. Mackay, A. Lakhtakia and W. S. Weiglhofer, Third-order implementation and convergence of the strong-property-fluctuation theory in electromagnetic homogenization, *Phys. Rev. E* 64 (2001) 066616.
- [61] F. Walbel, E. Ritter, and R. Linsbod, Properties of TiO_x films prepared by electron-beam evaporation of titanium and titanium suboxides, *Appl. Opt.* 42 (2003) 4590–4593.
- [62] H. A. Macleod, *Thin-film optical filters*, 3rd ed., Institute of Physics, Bristol, UK (2001).

- [63] I. Hodgkinson and Q. h. Wu, Birefringent thin films and polarizing elements, World Scientific, Singapore (1998).
- [64] S. Brunauer, P. H. Emmett and E. Teller, Adsorption of gasses in multimolecular layers, J. Am. Chem. Soc. 60 (1938) 309–319.
- [65] G. Bomchil, R. Herino, K. Barla and J. C. Pfister, Pore size distribution in porous silicon studied by adsorption isotherms, J. Electrochem. Soc. 130 (1983) 1611–1614.
- [66] J. V. Ryan, M. Horn, A. Lakhtakia and C. G. Pantano, Characterization of sculptured thin films, Proc. SPIE 5593 (2004) 643–649.
- [67] R. Messier, T. Takamori and R. Roy, Structure-composition variation in rf-sputtered films of Ge caused by process parameter changes, J. Vac. Sci. Technol. 13 (1976) 1060–1065.
- [68] J. R. Blanco, P. J. McMarr, J. E. Yehoda, K. Vedam and R. Messier, Density of amorphous germanium films by spectroscopic ellipsometry, J. Vac. Sci. Technol. A 4 (1986) 577–582.
- [69] I. Hodgkinson and Q. h. Wu, Inorganic chiral optical materials, Adv. Mater. 13 (2001) 889–897.
- [70] R. Messier, V. C. Venugopal and P. D. Sunal, Origin and evolution of sculptured thin films, J. Vac. Sci. Technol. A 18 (2000) 1538–1545.
- [71] A. C. V. Popta, J. C. Sit and M. J. Brett, Optical properties of porous helical thin films, Appl Opt, 43 (2004) 3632–3639.
- [72] V. C. Venugopal and A. Lakhtakia, in: O.N. Singh, A. Lakhtakia (Eds.), Electromagnetic fields in unconventional materials and structures, Wiley, New York (2000).
- [73] I. Hodgkinson, Q. h. Wu, B. Knight, A. Lakhtakia and K. Robbie, Vacuum deposition of chiral sculptured thin films with high optical activity, Appl Opt 39 (2000) 642–649.
- [74] T. G. Mackay, On extended homogenization formalisms for nanocomposites, J. Nanophoton. 2 (2008) 021850.
- [75] J. Van Kranendonk and J. E. Sipe, Foundations of the macroscopic electromagnetic theory of dielectric media, Prog. Opt. 15 (1977) 245–350.
- [76] M. T. Prinkey, A. Lakhtakia and B. Shanker, On the extended Maxwell–Garnett and the extended Bruggeman approaches for dielectric-in-dielectric composites, Optik 96 (1994) 25–30.

- [77] B. Shanker, A. Lakhtakia, Extended Maxwell Garnett model for chiral-in-chiral composites, *J. Phys. D: Appl. Phys.* 26 (1993) 1746–1758.
- [78] B. Shanker, The extended Bruggeman approach for chiral-in-chiral mixtures, *J. Phys. D: Appl. Phys.* 29 (1996) 281–288.
- [79] A. Lakhtakia and W. S. Weiglhofer, Green function for radiation and propagation in helicoidal bianisotropic mediums, *IEE Proc.–Microw. Antennas Propag.* 144 (1997) 57–59.
- [80] M. Born, E. Wolf, *Principles of optics*, 7th ed., Pergamon, Oxford, UK (1999), Appendix III.
- [81] F. Wang, Note on the asymptotic approximation of a double integral with an angular-spectrum representation, *Int. J. Electron. Commun. (AEÜ)* 59 (2005) 258–261.
- [82] M. D. Pickett, A. Lakhtakia and J. A. Polo Jr., Spectral responses of gyrotropic chiral sculptured thin films to obliquely incident plane waves, *Optik* 9 (2004) 393–398.
- [83] Z. D. Genchev, Anisotropic and gyrotropic version of Polder and van Santen's mixing formula, *Waves Random Media* 2 (1992) 99–110.
- [84] N. P. Zhuck, Strong-fluctuation theory for a mean electromagnetic field in a statistically homogeneous random medium with arbitrary anisotropy of electrical and statistical properties, *Phys. Rev. B* 50 (1994) 15636–15645.
- [85] E. Kretschmann, H. Raether, Radiative decay of nonradiative surface plasmons excited by light, *Z. Naturforsch. A* 23 (1968) 2135–2136.
- [86] A. Lakhtakia, Surface-plasmon wave at the planar interface of a metal film and a structurally chiral medium, *Opt. Commun.* 279 (2007) 291–297.
- [87] H. J. Simon, D. E. Mitchell and J. G. Watson, Surface plasmons in silver film — A novel undergraduate experiment, *Am. J. Phys.* 43 (1975) 630–636.
- [88] J. Homola, Present and future of surface plasmon resonance biosensors, *Anal. Bioanal. Chem.* 377 (2003) 528–539.
- [89] A. Shalabney, I. Abdulhalim, Sensitivity-enhancement methods for surface plasmon sensors, *Laser Photon. Rev.* 5 (2011) 571–606.

- [90] A. Shalabney, A. Lakhtakia, I. Abdulhalim, A. Lahav, Christian Patzig, I. Hazeek, A. Karabchevsky, B. Rauschenbach, F. Zhang, J. Xu Surface plasmon resonance from metallic columnar thin films, *Photon. Nanostruct. Fundam. Appl.* 7 (2009) 176–185.
- [91] A. Shalabney, C. Khare, B. Rauschenbach, I. Abdulhalim, Sensitivity of surface plasmon resonance sensors based on metallic columnar thin films in the spectral and angular interrogations, *Sensors Actuators B* 159 (2011) 201–212.
- [92] I. Abdulhalim II, A. Lakhtakia, A. Lahav, F. Zhang, J. Xu, Porosity effect on surface plasmon resonance from metallic sculptured thin films, *Proc. SPIE* 7041 (2008) 70410C.
- [93] T. G. Mackay, On the sensitivity of generic porous optical sensors, *Appl. Optics* 51 (2012) 2752–2758.
- [94] S. A. Maier, *Plasmonics: Fundamentals and applications*, Springer, New York, NY, USA (2007).
- [95] M. A. Motyka and A. Lakhtakia, Multiple trains of same-color surface plasmon-polaritons guided by the planar interface of a metal and a sculptured nematic thin film, *J. Nanophoton.* 2 (2008) 021910.
- [96] Z. Salamon, G. Lindblom and G. Tollin, Plasmon-waveguide resonance and impedance spectroscopy studies of the interaction between penetratin and supposed lipid bilayer membranes, *Biophysical J.* 84 (2003) 1796–1807.
- [97] M. A. Motyka, A. Lakhtakia, Multiple trains of same-color surface plasmon-polaritons guided by the planar interface of a metal and a sculptured nematic thin film, Part II: Arbitrary incidence, *J. Nanophoton.* 3 (2009) 033502.
- [98] J. A. Polo Jr. and A. Lakhtakia, On the surface plasmon polariton wave at the planar interface of a metal and a chiral sculptured thin film, *Proc. R. Soc. Lond. A.* 465 (2009) 87–107.
- [99] M. Faryad and A. Lakhtakia, On surface plasmon-polariton waves guided by the interface of a metal and a rugate filter with sinusoidal refractive-index profile, *J. Opt. Soc. Am. B.* 27 (2010) 2218–2223.
- [100] A. Lakhtakia, Surface multiplasmonics, *Proc. SPIE* 8104 (2011) 810403.
- [101] Devender, D. P. Pulsifer and A. Lakhtakia, Multiple surface plasmon polariton waves, *Electron. Lett.* 45 (2009) 1137–1138.

- [102] T. H. Gilani, N. Duskhkina, W. L. Freeman, M. Z. Numan, D. N. Talwar and D. P. Pulsifer, Surface plasmon resonance due to the interface of a metal and a chiral sculptured thin film, *Opt. Eng.* 49 (2010) 120503.
- [103] A. Lakhtakia, Y.-J. Jen and C.-F. Lin, Multiple trains of same-color surface plasmon-polaritons guided by the planar interface of a metal and a sculptured nematic thin film. Part III: Experimental evidence, *J. Nanophoton.* 3 (2009) 033506.
- [104] S. M. Pursel, and M. W. Horn, Prospects for nanowire sculptured-thin-film devices, *J. Vac. Sci. Technol. B* 25 (2007) 2611–2615.
- [105] Y. J. Liu, Shi., J., F. Zhang, H. Liang, J. Xu, A. Lakhtakia, S. J. Fonash and T. J. Huang, High-speed optical humidity sensors based on chiral sculptured thin films, *Sens. Actuat. B: Chem.* 156 (2011) 593–598.
- [106] I. J. Hodgkinson, Q. H. Wu, K. E. Thorn, A. Lakhtakia and M. W. McCall, Spacerless circular-polarization spectral-hole filters using chiral sculptured thin films: theory and experiment, *Opt. Commun.* 184 (2000) 57–66.
- [107] A. Lakhtakia, M. W. McCall and J. A. Sherwin, Q. H. Wu and I. J. Hodgkinson, Sculptured-thin-film spectral holes for optical sensing of fluids, *Opt. Commun.* 194 (2001) 33–46.
- [108] T. Turbadar, Complete absorption of light by thin metal films, *Proc. Phys. Soc. Lond.* 73 (1959) 40–44.
- [109] A. Lakhtakia, Surface-plasmon wave at the planar interface of a metal film and a structurally chiral medium, *Opt. Commun.* 279 (2007) 291–297.
- [110] A. Lakhtakia, Pseudo-isotropic and maximum-bandwidth points for axially excited chiral sculptured thin films, *Microw. Opt. Technol. Lett.* 34 (2002) 367–371.
- [111] F. Wang and A. Lakhtakia, Optical crossover phenomenon due to a central 90° -twist defect in a chiral sculptured thin film or chiral liquid crystal, *Proc. R. Soc. Lond. A* 461 (2005) 2985–3004.
- [112] I. Abdulhalim, M. Zourob and A. Lakhtakia, Surface plasmon resonance for biosensing: A mini review, *Electromagnetics* 28 (2008) 214–242.
- [113] J. A. Polo Jr. and A. Lakhtakia, Surface electromagnetic waves: A review, *Laser Photon. Rev.* 5 (2011) 234–246.

- [114] A. D. Boardman, Electromagnetic surface modes, J. Wiley, Chichester, New York, USA, 1982.
- [115] A. Otto, Excitation of nonradiative surface plasma waves in silver by the method of frustrated total reflection, Z. Phys. 216 (1968) 398–410.
- [116] I. Abdulhalim, Surface plasmon TE and TM waves at the anisotropic film–metal interface, J. Opt. A, Pure Appl. Opt. 11 (2009) 015002.

